1D spatially chirped periodic structures: managing their spatial spectrum and investigating their near-field diffraction

MOHAMMADREZA ZAREI,[1] DAVUD HEBRI,[1] AND SAIFOLLAH RASOULI[1,2,*] (iD)

[1]*Department of Physics, Institute for Advanced Studies in Basic Sciences(IASBS), Zanjan 45137-66731, Iran*
[2]*Optics Research Center, Institute for Advanced Studies in Basic Sciences (IASBS), Zanjan 45137-66731, Iran*
*Corresponding author: rasouli@iasbs.ac.ir

This work introduces a class of 1D spatial-frequency-modulated structures with transmittance $T(x)$, in which the period changes along the x axis so that the corresponding spatial frequency $f(x)$ sinusoidally alternates between two values. It is shown that $T(x)$ generally is an almost-periodic function and has an impulsive spatial spectrum. However, we find the condition under which $T(x)$ is a periodic function and its spatial spectrum form a lattice of impulses. When the periodicity condition is fulfilled, we call these structures as 1D spatially chirped periodic structures. These structures are characterized by two natural numbers, named as n_c and n_{av}, and a real parameter named as frequency modulation strength (FMS). As an important special case, we define a 1D spatially chirped amplitude sinusoidal grating (SCASG) based on the transmission function of a conventional amplitude sinusoidal grating, in which the phase of conventional amplitude sinusoidal grating is replaced by desired chirped phase. Then the spatial spectrum of a 1D SCASG is investigated in detail, and it is shown that the spatial spectrum can be managed by changing the value of FMS. In other words, the grating's spectrum can be manipulated by adjusting the value of FMS. This feature might find applications in optical sharing of the incident power among different diffraction orders. Moreover, near-field diffraction from 1D SCASGs is studied by using the so-called angular (spatial) spectrum method, and Talbot distances for these gratings are determined and verified experimentally. It is shown that the intensity profiles at quartet- and octant-Talbot distances strongly depend on the values of the parameters n_c and n_{av}. In comparison with the conventional gratings, we see some new and interesting aspects in the diffraction from 1D SCASGs. For instance, unlike the conventional gratings, in some propagation distances, the diffraction patterns possess sharp and smooth intensity bars at which the intensity is several times of the incident light beam's intensity. It is shown that the maximum intensity of these bright bars over the diffraction patterns depends on the characteristic parameters of the grating, including n_c, n_{av}, and FMS of the grating. These intensity bars might find applications for trapping and aggregation of particles along straight lines. © 2022 Optica Publishing Group

1. INTRODUCTION

In optics, periodic structures play an essential role in many applications. Self-imaging, also known as the Talbot effect, is a well-known phenomenon in the diffraction of a plane wave from a periodic structure. For more than half a century, the physics of diffraction from 1D conventional periodic structures has attracted much attention, and many studies have allocated it [1–15]. For the first time, the Talbot effect was observed for the spatially periodic structures [16], and consequently it was studied on wavefronts having periodic structure [17]. Continuing, the Talbot effect has been generalized to periodic functions of other variables, including time [18,19], frequency [20], and angular frequency [21]. The Talbot effect in polar coordinates has been also studied [22,23]. Diffraction from

periodic structures has been used for characterization of optical vortices [24], generation of optical lattices [25–29], and vortex beam multiplication [30–34]. Diffraction from azimuthally periodic (radial) structures has been used for the generation of some structured beams [35–38] and measurement of the topological charge of vortex beams [39]. In addition, recently some other works on the Talbot effect have been studied [40–45].

Consider a transparent sheet having harmonic transmittance in which its period (and spatial frequency) varies continuously and slowly with the position. Such a structure is considered as a spatial-frequency-modulated structure [46]. The most well-known spatial-frequency-modulated structures are Fresnel zone plate and 1D zone plate. The phase of a Fresnel zone plate is proportional with r^2; therefore, spatial frequency along the radial coordinate is proportional with r, where r is the radial

coordinate. Moreover, the phase and spatial frequency of a 1D zone plate are proportional with x^2 and x, respectively. Recently a class of structures, named as quadratic curved-line (parabolic-line) gratings, has been introduced in which the phase is proportional with $(x - \gamma y^2)$, where (x, y) indicates Cartesian coordinates [47]. Therefore, spatial frequency along the x axis is constant, like a conventional grating, and along the y axis it is proportional with y, similar to a 1D zone plate. This kind of grating has been used as a simple and efficient tool for characterization of optical vortices [47–49].

In this work, we introduce a new class of spatial-frequency-modulated structures, named as spatially chirped structures, in which the spatial frequency has a sinusoidal functionality and alternates between two values, say f_1 and f_2. It is shown that the transmittance of these structures is an almost-periodic function in the general case. Nevertheless, we find the condition under which the transmittance is a periodic function. Under the obtained condition, the spatially chirped periodic structure can be fully determined with two natural numbers (n_c and n_{av}) and a real parameter named as FMS, which is proportional with $f_1 - f_2$. Based on the transmission function of a conventional amplitude sinusoidal grating, a 1D SCASG is defined, and its spatial spectrum is investigated in detail. It is shown that the spatial spectrum of 1D SCASGs can be managed by adjusting the value of FMS. Furthermore, near-field diffraction from 1D SCASGs is investigated, and it is shown that the intensity profiles at the fractional Talbot distances, namely quartet- and octant-Talbot distances, strongly depend on the values of n_c and n_{av}. It is also shown that the diffraction patterns at some distances from the grating include bright bars having sharp and smooth profiles where the intensity is higher than the incident beam's intensity. By adjusting the value of FMS, the intensity of these bright bars can be maximized and reaches to several times of the intensity of the incident beam. This feature might find applications in trapping and aggregation of particles along straight lines.

It is worth noting that, in recent years, both temporally chirped light fields and spatially chirped structures have been used for various applications in science and technology. Here, we review some applications. The filter response of non-uniform, almost-periodic structures, such as corrugated optical waveguides, has been theoretically predicted in [50]. The use of a linearly chirped Bragg grating filter for dispersion cancellation has been proposed in [51]. On the other hand, a chirped-quasi-periodic structure has been proposed for both multiple quasi-phase-matching and multiple bandwidths control [52]. In another work, an optical superlattice with a chirped dual periodic structure has been designed and used for generation of tunable vortex beams in the blue spectral range [53]. Moreover, by using a gradually changing period grating, a method for measuring orbital angular momentum states of light beams has been reported [54]. In laser manufacturing, the spatially chirped gratings have been used to improve the optical bistability on reflection from distributed feedback semiconductor laser amplifiers [55] and to enhance the wavelength tunability in the distributed feedback lasers [56]. Finally, we address in another work that a chirped moiré fiber Bragg grating has been used for measuring the magnitude, position, and footprint of a transverse load [57].

Because of the existence of an intense analogy between time domain and spatial domain phenomena in optical sciences, such as the temporal and spatial Talbot effect [58–61], and considering a wide range of applications of some of the chirped structures that we have reviewed, we think that the spatially chirped periodic structures and their Talbot effect might find applications in the spatial domain.

2. 1D SPATIALLY CHIRPED STRUCTURES

As the simplest form of 1D periodic structures, a 1D amplitude sinusoidal grating is indicated by the following transmission function [62,63]:

$$T_0(x) = \cos^2\left(\frac{\varphi_0(x)}{2}\right) = \frac{1}{2}\left[1 + \cos(\varphi_0(x))\right], \quad (1)$$

where $\varphi_0(x) = \frac{2\pi}{p_0}x = 2\pi f_0 x$ denotes the phase over the grating in which p_0 and $f_0 = \frac{1}{p_0}$ are the fundamental period and frequency, respectively. The lateral extension of the grating is considered infinite. Now let us define a grating with a spatially variable period, for which the period alternates between two values p_1 and p_2; therefore, the spatial frequency alternates between two values $f_1 = \frac{1}{p_1}$ and $f_2 = \frac{1}{p_2}$. Hereafter, we suppose that $p_1 < p_2$ and, thus, $f_1 > f_2$. As at different positions the spatial frequency changes between f_1 and f_2, we consider $f(x)$ as the spatial frequency envelope. It is noteworthy that frequency modulation in the time domain is fully described for signals [64,65]. Here, we consider the sinusoidal form for $f(x)$ changing between f_1 and f_2 with a period p_c, and we have

$$f(x) = f_{av} + \delta f \cos(2\pi f_c x), \quad (2)$$

where $f_c = \frac{1}{p_c}$ can be called as the chirping frequency, f_{av} is the average frequency given by

$$f_{av} = \frac{f_1 + f_2}{2} = \frac{1}{2}\left(\frac{1}{p_1} + \frac{1}{p_2}\right), \quad (3)$$

and δf is frequency modulation amplitude, defined by

$$\delta f = \frac{f_1 - f_2}{2} = \frac{1}{2}\left(\frac{1}{p_1} - \frac{1}{p_2}\right). \quad (4)$$

Now the average period of the grating can be defined by the inverse of the average frequency:

$$p_{av} = \frac{1}{f_{av}} = \frac{2p_1 p_2}{p_1 + p_2}. \quad (5)$$

Considering Eq. (3), we have $f_2 < f_{av} < f_1$ and, therefore, $p_1 < p_{av} < p_2$. In this work, we assume that the chirping period is larger than or equal to the average period of the grating, namely $p_c \geq p_{av}$. The phase of the chirped grating $\varphi(x)$ can be obtained by $f(x) = \frac{1}{2\pi}\frac{d\varphi(x)}{dx}$, or equally by

$$\varphi(x) = 2\pi \int f(x)dx. \quad (6)$$

Substituting Eq. (2) into Eq. (6), we have

$$\varphi(x) = 2\pi f_{av} x + k \sin(2\pi f_c x), \quad (7)$$

where $k = \frac{\delta f}{f_c}$, and we call it frequency modulation strength (FMS). As is apparent, the chirping phase $\varphi(x)$ is characterized by three parameters: f_{av}, f_c, and δf. The extremum values of δf can be obtained by considering Eqs. (3) and (4). The minimum possible value is $\delta f = 0$, which means that there is not frequency modulation ($f_1 = f_2$ and equivalently $p_1 = p_2$). The maximum possible value is $\delta f = f_{av} = f_1/2$, which means $f_2 = 0$ and equivalently $p_2 = \infty$. Therefore, we have $0 \leq \delta f \leq f_{av}$ and equivalently

$$0 \leq k \leq \frac{f_{av}}{f_c}. \qquad (8)$$

Equation (8) determines the variation interval of the FMS.

Indeed, Eq. (7) introduces the chirping phase, which can be used for defining the transmission function of a 1D spatially chirped structure, $T(x)$, as follows:

$$T(x) = \mathrm{Pe}\,[\varphi(x)], \qquad (9)$$

where $\mathrm{Pe}(u)$ is an arbitrary periodic function with fundamental period 2π so that $\mathrm{Pe}(u + 2n\pi) = \mathrm{Pe}(u)$ for any integer n.

3. 1D SPATIALLY CHIRPED PERIODIC STRUCTURES

Now let us consider two questions about the transmission function of a 1D spatially chirped structure: When is $T(x)$ a periodic function? If it is, what is the period? Assuming that $T(x)$ is a periodic function with a period p, namely $T(x + p) = T(x)$, we have

$$\varphi(x + p) = \varphi(x) + 2n\pi, \qquad (10)$$

where n is an integer. Thus, if Eq. (10) is satisfied, $T(x)$ is periodic function with a period p. Using Eq. (7), we get

$$\varphi(x + p) = 2\pi f_{av}(x + p) + k \sin(2\pi f_c (x + p)). \qquad (11)$$

If p is an integer multiple of p_c, say $p = n_c p_c$, and considering $p_c = \frac{1}{f_c}$, we have $p f_c = n_c$ and, therefore, $\sin(2\pi f_c(x + p)) = \sin(2\pi f_c x)$. In this case, Eq. (11) reduces to

$$\varphi(x + p) = \varphi(x) + 2\pi f_{av} p, \qquad (12)$$

where we used the definition of $\varphi(x)$, namely Eq. (7). Comparing Eqs. (10) and (12), one can deduce that Eq. (10) is satisfied if $f_{av} p$ is an integer number, say $f_{av} p = n_{av}$, and considering $f_{av} = \frac{1}{p_{av}}$, p is an integer multiple of p_{av}, say $p = n_{av} p_{av}$. The obtained two conditions: $p = n_{av} p_{av}$ and $p = n_c p_c$, can be merged as $n_c p_c = n_{av} p_{av}$, which can be rewritten as follows:

$$\frac{f_{av}}{f_c} = \frac{p_c}{p_{av}} = \frac{n_{av}}{n_c}, \qquad (13)$$

where n_c and n_{av} are two coprime natural numbers. Equation (13) means that p_c and p_{av} are commensurable, i.e., $\frac{p_c}{p_{av}}$ is a rational number. In summary, $T(x)$ is a periodic function if p_c and p_{av} are commensurable; namely, there exist two coprime natural numbers n_c and n_{av} such that $n_c p_c = n_{av} p_{av}$. In this case, the fundamental period of $T(x)$

is obtained as $p = n_c p_c = p_{av} n_{av}$, and inverting each side, the fundamental frequency is also obtained as $f = \frac{f_c}{n_c} = \frac{f_{av}}{n_{av}}$. It should be mentioned that, as $p_c \geq p_{av}$, we have $n_{av} \geq n_c$. Moreover, by substituting $\frac{f_{av}}{f_c}$ from Eq. (13) in Eq. (8), we get

$$0 \leq k \leq \frac{n_{av}}{n_c}. \qquad (14)$$

4. 1D SPATIALLY CHIRPED AMPLITUDE SINUSOIDAL GRATING

As a simple and important example of 1D spatially chirped structures, we define the 1D spatially chirped amplitude sinusoidal grating (SCASG) by considering $\mathrm{Pe}(u) = \cos^2(\frac{u}{2})$. In other words, the transmission function of this grating can be obtained by replacing $\varphi_0(x)$ by $\varphi(x)$ in Eq. (1) as follows:

$$T(x) = \cos^2\left(\frac{\varphi(x)}{2}\right) = \frac{1}{2}[1 + \cos(\varphi(x))], \qquad (15)$$

where $\varphi(x)$ is the chirping phase defined by Eq. (7).

To clarify the matter, we investigate some practical examples. As the first example, let us consider a grating with $p_1 = 0.1$ mm, $p_2 = 0.3$ mm. Substituting these values in Eq. (5), we get $p_{av} = 0.15$ mm. Now considering different values for n_c and n_{av} and substituting in Eq. (13), we get different values for p_c. Using these parameters, we construct different 1D SCASGs. In Fig. 1, the transmission functions and the corresponding frequency envelopes of the gratings having $n_c = 1$ and $n_c = 2$ for different values of n_{av} are illustrated. As is seen, the number of frequency envelopes and the number of transmission function peaks, in each period, are equal to n_c and n_{av}, respectively.

As the second example, we consider a grating with $p_{av} = 0.1$ mm, $p_c = 0.4$ mm ($n_{av} = 4$, $n_c = 1$), and different values of k. Therefore, we construct 1D SCASGs having different FMSs. In Fig. 2, the transmission functions and the corresponding frequency envelopes of the gratings having $k = 0, 1, 2, 3$, and 4 are illustrated (see Visualization 1).

A. Spatial Spectrum of a 1D SCASG

Now let us derive the spatial spectrum of a 1D SCASG. For this purpose, first, we rewrite Eq. (15) in the following form:

$$T(x) = \frac{1}{2} + \frac{1}{4}[\exp(i\varphi(x)) + \exp(-i\varphi(x))]. \qquad (16)$$

Substituting $\varphi(x)$ from Eq. (7) in Eq. (16), and using the Jacobi–Anger identity [66],

$$\exp(i\gamma \sin(x)) = \sum_{m=-\infty}^{+\infty} J_m(\gamma) \exp(imx), \qquad (17)$$

we obtain

$$\exp(i\varphi(x)) = \sum_{m=-\infty}^{+\infty} J_m(k) \exp(i2\pi f_m x), \qquad (18a)$$

$$\exp(-i\varphi(x)) = \sum_{m=-\infty}^{+\infty} J_m(k) \exp(-i2\pi f_m x), \qquad (18b)$$
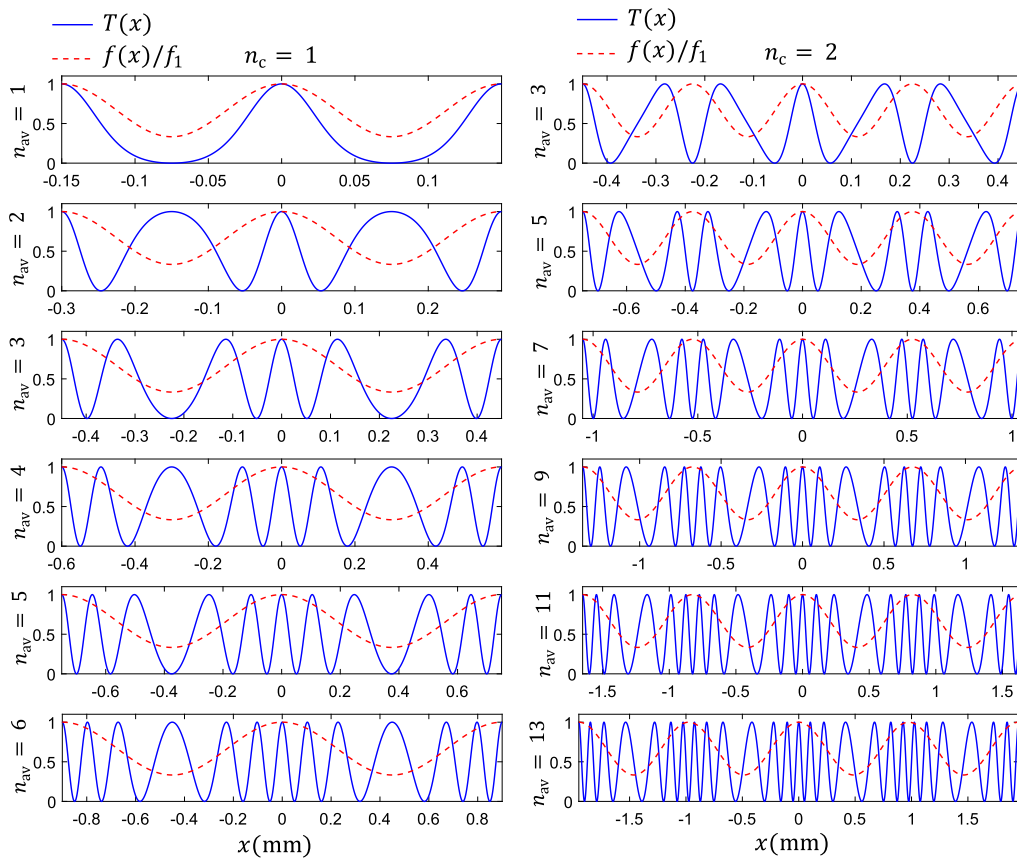
Fig. 1. Transmission and frequency envelope functions of 1D SCASGs, having $p_1 = 0.1$ mm, $p_2 = 0.3$ mm, and $p_{av} = 0.15$ mm with $n_c = 1$ (first column) and $n_c = 2$ (second column) for different values of n_{av}. All plots are depicted in an interval of $[-p, p]$.
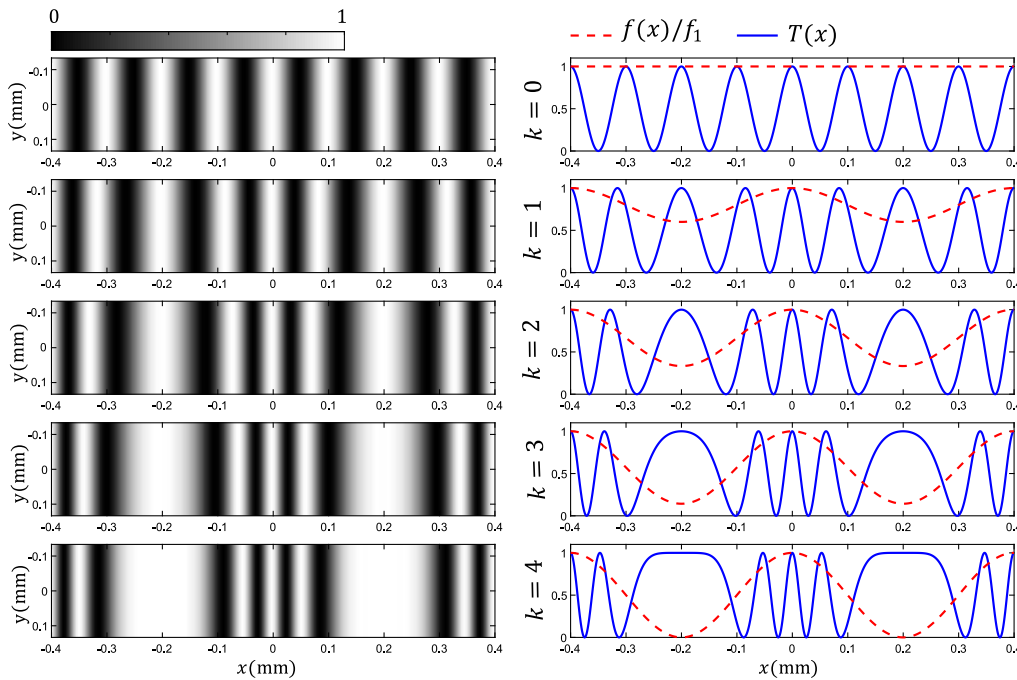

Fig. 2. First column, transmittance of 1D SCASGs having $p_{av} = 0.1$ mm, $p_c = 0.4$ mm, $n_{av} = 4$, and $n_c = 1$ with different values of FMS. Second row, the corresponding transmission profiles (solid blue plots) and the frequency envelope functions (dashes red plots). All patterns are illustrated in $[-p, p]$ interval (see Visualization 1).

where $f_m = f_{av} + m f_c$. Now by substituting Eq. (18) in Eq. (16), we have

$$T(x) = \frac{1}{2} + \frac{1}{4}\left\{\sum_{m=-\infty}^{+\infty} J_m(k)\left[e^{i2\pi f_m x} + e^{-i2\pi f_m x}\right]\right\}, \quad \textbf{(19)}$$

or equally

$$T(x) = \frac{1}{2}\left\{1 + \sum_{m=-\infty}^{+\infty} J_m(k)\cos(2\pi f_m x)\right\}. \quad \textbf{(20)}$$

Now it is easy to obtain the spatial spectrum of $T(x)$ by calculating the Fourier transform of Eq. (19), and the result is

$$\tilde{T}(\xi) = \frac{1}{2}\delta(\xi) + \frac{1}{4}\left\{\sum_{m=-\infty}^{+\infty} J_m(k)\left[\delta(\xi - f_m) + \delta(\xi + f_m)\right]\right\}, \quad \textbf{(21)}$$

where δ denotes the Dirac delta function. Comparing Eqs. (19) and (21) with Eqs. (A4) and (A6), respectively, shows that $T(x)$ is in general an almost-periodic function. As is apparent, the spatial spectrum of the grating consists of a set of discrete impulses that, in general, is not a 1D lattice. Therefore, in a general case, $T(x)$ is an almost-periodic function (see Appendix A). However, when Eq. (13) is satisfied, $T(x)$ is a periodic function with a fundamental period of $p = n_c p_c = n_{av} p_{av}$ and spatial frequency of $f = \frac{f_c}{n_c} = \frac{f_{av}}{n_{av}}$. In this case, Eq. (20) reduces to

$$\tilde{T}(\xi) = \frac{1}{4}\left\{2\delta(\xi) + \sum_{m=-\infty}^{+\infty} J_m(k)[\delta(\xi - lf) + \delta(\xi + lf)]\right\}, \quad \textbf{(22)}$$

where $l = n_{av} + m n_c$ are integer numbers. As is expected, in this case, the spatial spectrum of the grating is a set of impulses, and they form a 1D lattice [compare Eqs. (22) and (A3)]. Furthermore, comparing Eqs. (22) and (A3), the amplitude of impulses can be obtained. First of all, let us obtain the amplitude of the DC impulse. By setting $l = 0$, we get $m = -\frac{n_{av}}{n_c}$. As n_{av} and n_c are two coprime natural numbers and m is an integer, the $m = -\frac{n_{av}}{n_c}$ equality is only possible if $n_c = 1$. Therefore, A_0, the amplitude of the DC impulse, can be expressed as follows:

$$A_0 = \begin{cases} \frac{1}{2}\left[1 + (-1)^{n_{av}} J_{n_{av}}(k)\right] & \text{if} \quad n_c = 1, \\ \frac{1}{2} & \text{if} \quad n_c > 1, \end{cases} \quad \textbf{(23)}$$

where we used $J_{-m}(k) = (-1)^m J_m(k)$. Figsures 3(a) and 3(b) show plots of different orders of the Bessel functions, and the table in Fig. 3(c) shows the Bessel functions' arguments in which their values (first row) or the values of their first derivatives (second row) reach zero. According to Eq. (23), only for the case $n_c = 1$, the amplitude of the DC impulse depends on k; otherwise, it is constant. Using Eq. (14) when $n_c = 1$, we have $0 \leq k \leq n_{av}$, and in this interval $J_{n_{av}}(k)$ is an ascending positive function [see Fig. 3 (we verified this feature up to $n_{av} = 200$ numerically)].

In this case, if n_{av} is an even (odd) number, A_0 is an ascending (descending) function of k. In addition, when n_{av} is an even (odd) number, A_0 is larger (smaller) than $\frac{1}{2}$.

The amplitude of the higher order impulses ($l \neq 0$) is obtained using Eq. (22) and considering $l = n_{av} + m n_c$ as follows:
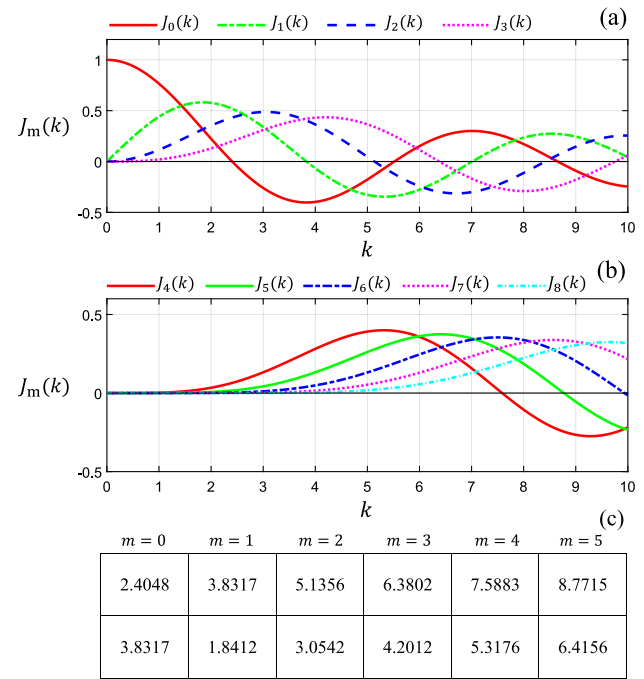
Fig. 3. (a) and (b) Plots of different orders of the Bessel functions, and (c) the Bessel functions' arguments in which their values (first row) or the values of their first derivatives (second row) reach zero.

Table 1. Values of r and s Determining Amplitudes of Different Order Impulses for a 1D SCASG Having $n_{av} = 3$ and $n_c = 1$

l	±1	±2	±3	±4	±5	±6	±7	±8
r	2	−1	0	1	2	3	4	5
s	4	−5	6	7	8	−9	10	−11

$$A_l = \frac{J_r(k) + J_s(k)}{4}, \quad \textbf{(24)}$$

provided that $r = \frac{l - n_{av}}{n_c}$ and $s = -\frac{l + n_{av}}{n_c}$ are two integer numbers. If both r and s are not integer numbers, then the spectrum does not include the l-order impulse. If only one of r or s, say r, is an integer number, then Eq. (24) gets the following form: $A_l = \frac{J_r(k)}{4}$.

As a typical example, we consider a grating with $n_c = 1$ and $n_{av} = 3$, presented in the first column, third row of Fig. 1. In this case, using Eq. (23), we obtain the amplitude of the DC impulse as $A_0 = \frac{1}{2}(1 - J_3(k))$. Setting $l = \pm 1$ in $l = 3 + m$, we get $m = -2$ and $m = -4$, and then the amplitude of the first-order impulses can be obtained as $A_{\pm 1} = \frac{1}{4}(J_2(k) + J_4(k))$, in which $J_{-m}(k) = (-1)^m J_m(k)$ is also used. Similarly, the amplitudes of the higher order impulses can be obtained, and the results are shown in Table 1. By substituting the values of r and s from the table in Eq. (24), the amplitudes of different order impulses can be determined. In the use of values presented in Table 1, we always consider $J_{-m}(k) = (-1)^m J_m(k)$. For example, for the values presented in the fifth column ($l = \pm 4, r = 1, s = -7$ of the table) we have $A_{\pm 4} = \frac{1}{4}(J_1(k) + J_{-7}(k)) = \frac{1}{4}(J_1(k) - J_7(k))$.

As another typical example, we consider a grating with $n_c = 2$ and $n_{av} = 7$, shown in the second column, third row
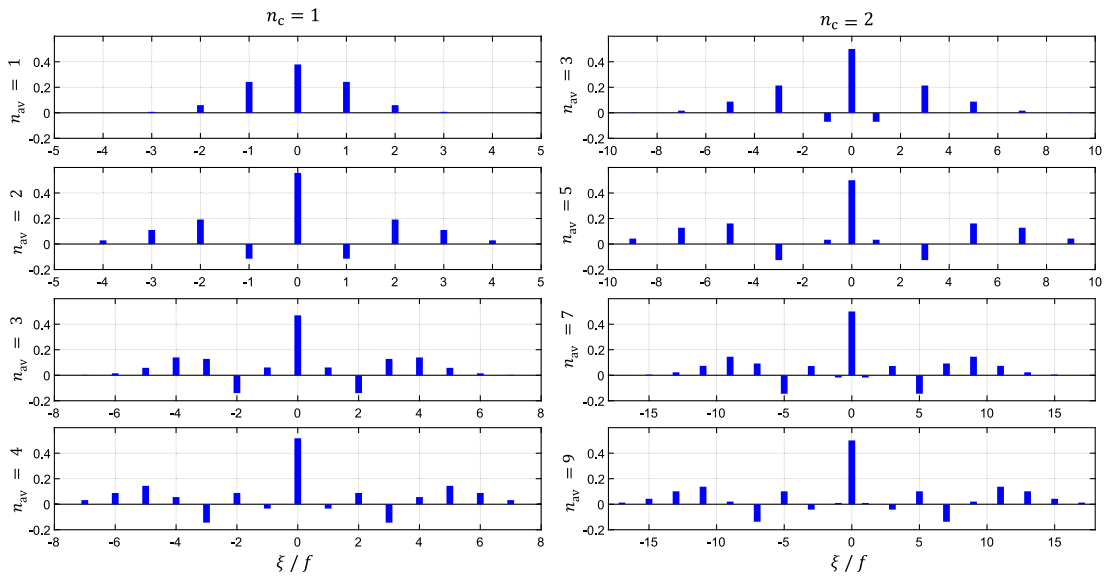
Fig. 4. The amplitude of the impulses in the spectra of gratings is shown in the first and second columns of Fig. 1.

Table 2. Values of r and s Determining Amplitudes of Different Order Impulses for a 1D SCASG Having $n_{av} = 7$ and $n_c = 2$

l	±1	±3	±5	±7	±9	±11	±13	±15	±17
r	-3	2	-1	0	1	2	3	4	5
s	4	-5	6	-7	8	-9	10	-11	12

of Fig. 1. According to Eq. (23), the amplitude of the DC impulse $A_0 = \frac{1}{2}$, and according to Eq. (24), amplitudes of other impulses are presented in Table 2. As is apparent, except for the DC impulse, the spectrum includes only odd-order impulses. This feature is established for the case $n_c = 2$ generally.

In summary, according to Eq. (24), the amplitudes of the impulses (except the DC impulse) in the gratings' spectrum are proportional to $J_r(k) + J_s(k)$. Therefore, by considering appropriate values for k, in which $J_r(k) + J_s(k)$ is zero or maximum, one can remove/maximize some impulses from the spectrum of the grating. This fact might have some applications in the manipulation of the grating spectrum.

In Fig. 4, the corresponding impulse combs of the gratings shown in Fig. 1 are illustrated. As is expected, in the first column ($n_c = 1$), the amplitude of the DC impulse is larger (smaller) than $\frac{1}{2}$ for even (odd) values of n_{av}, and in the second column ($n_c = 2$), the amplitude of the DC impulse is equal to $\frac{1}{2}$ for all values of n_{av}. In the second column, we only have impulses with odd orders (except the DC impulse). This feature can be easily explained by $l = n_{av} + mn_c$. Another important feature is that, by increasing the value of n_{av}, the number of impulses with considerable values of amplitude increases.

Figure 5 shows the corresponding impulse combs of the gratings presented in Fig. 2. This figure shows the absolute values of the impulses' amplitudes. By increasing the FMS, higher order Bessel functions participate in the spatial spectrum. Therefore, the number of impulses with considerable amplitudes increases. The background Visualization 2 of Fig. 5 shows the evolution of transmission profile, frequency envelope
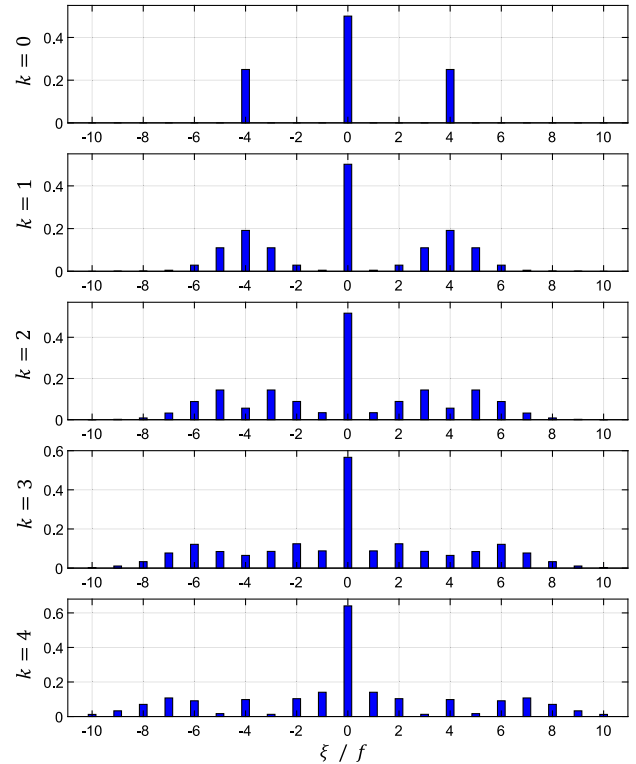

Fig. 5. Absolute values of impulses' amplitudes for the spectra of the gratings shown in Fig. 2 (see Visualization 2).

function, and spatial spectrum of a 1D SCASG under variation of FMS. As is apparent by increasing the value of k, the width of the frequency spectrum increases. It is also seen that, by changing the value of k, some impulses can be removed, or some impulses can be locally maximized. This feature might find some applications for intensity sharing among different diffraction orders of the gratings. In other words, the spatial spectrum of the grating can be managed by changing the values
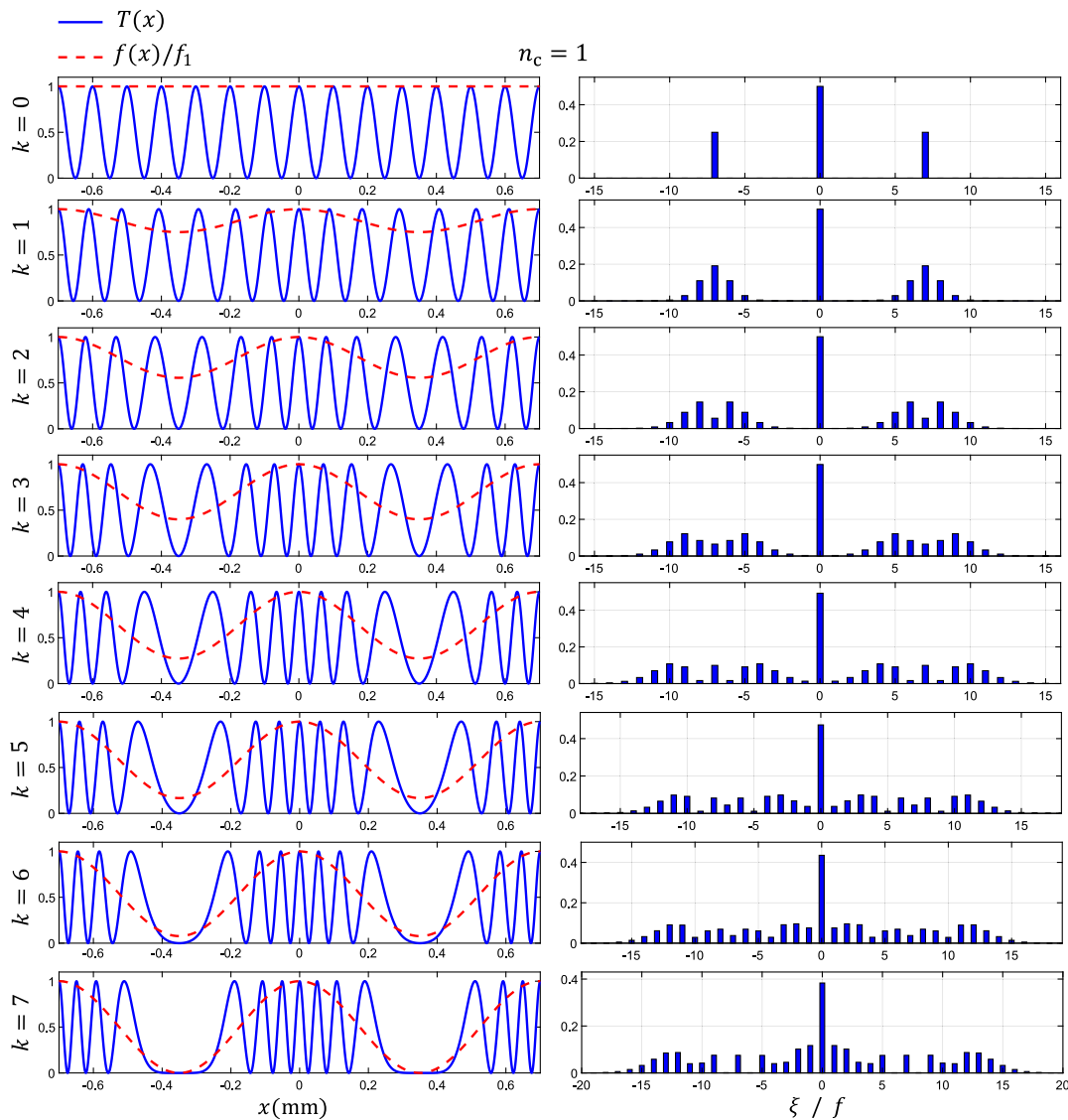
Fig. 6.   First column, transmission and frequency envelope functions of the gratings with $p_{av} = 0.1$ mm, $n_{av} = 7$, and $n_c = 1$ having different values of FMS. Second column, absolute values of impulses' amplitudes for the spectra of the gratings presented in the first column (see Visualization 3).

of FMS. It is worth mentioning that, in another work, with the aid of adjustable amplitude-phase hybrid gratings, intensity-sharing management among diffraction orders was previously proposed [67].

In Fig. 6, we consider a set of gratings with $p_{av} = 0.1$ mm, $n_{av} = 7$, and $n_c = 1$ having different values of FMS. According to Eq. (14), the maximum possible value of k is 7. The transmission and frequency envelope functions are plotted in the first column, and the corresponding impulse combs are illustrated in the second column. Here again, by increasing k, the number of impulses with considerable amplitudes increases.

In Fig. 7, a set of gratings with $p_{av} = 0.1$ mm, $n_{av} = 7$, and $n_c = 2$ having different values of FMS is considered. The maximum possible value of k is 3.5, according to Eq. (14). The first column shows the transmission and frequency envelope functions, and the second column illustrates the corresponding impulse combs. Here also, the number of impulses with considerable amplitudes increases by increasing the value of FMS.

Furthermore, comparing the first to fourth rows of Figs. 6 and 7 having the same values of k, we see that in each row the spatial spectrum in Fig. 7 is wider than the spatial spectra in Fig. 6 (see Visualization 3 and Visualization 4).

Figure 8, first column, illustrates the variation of amplitudes of some impulses in the spectrum of a 1D SCASG having $n_{av} = 3$ and $n_c = 1$, in terms of FMS. The second column shows the impulse combs for three different values of FMS. As n_{av} is an odd number, the amplitude of the DC impulse, A_0, is a descending function of k, and its value is always less than $\frac{1}{2}$. The amplitude of the third-order impulse $A_{\pm n_{av}} = A_{\pm 3}$ (see first row) decreases by increasing k and reaches to zero at $k = 2.4115$, then increases. According to Table 1, $A_{\pm 3} = \frac{1}{4}(J_0(k) + J_6(k))$. As the value of $J_6(k)$ in the interval of $0 \le k \le 3$ is almost negligible (see Fig. 3), then $A_{\pm 3} \approx \frac{J_0(k)}{4}$. To determine the accuracy of this approximation, compare the first zero of $J_0(k)$, $k = 2.4048$ with the
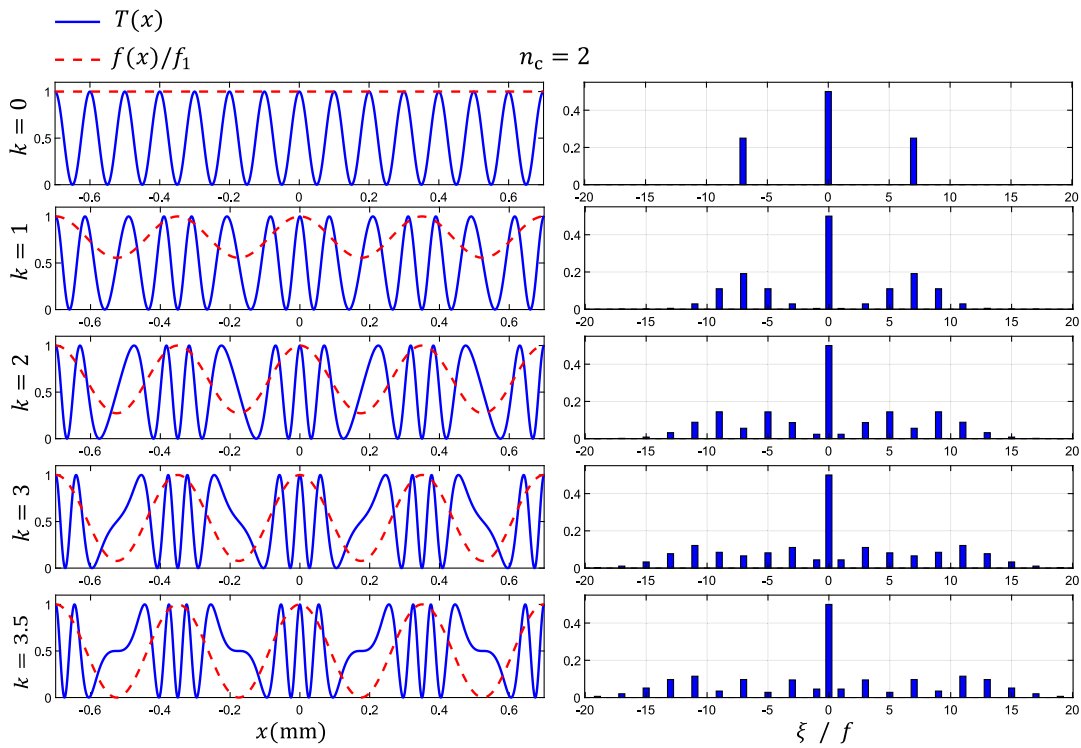
Fig. 7. First column, transmission and frequency envelope functions of the gratings with $p_{av} = 0.1$ mm, $n_{av} = 7$, and $n_c = 2$ having different values of FMS. Second column, absolute values of impulses' amplitudes for the spectra of the gratings presented in the first column (see Visualization 4).
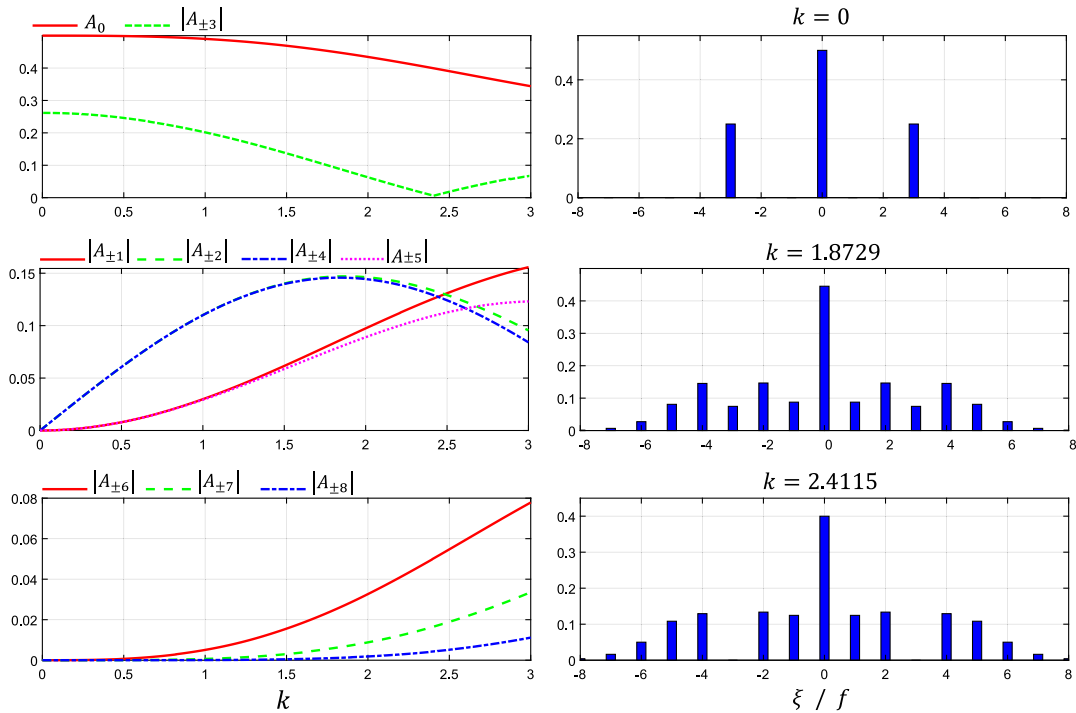

Fig. 8. Variation of different impulse amplitudes of a 1D SCASG having $n_{av} = 3$ and $n_c = 1$, in terms of FMS (first column). Absolute values of different impulse amplitudes of three gratings with different given values of FMS (second column); see Visualization 5.

root of A_0, $k = 2.4115$. The amplitudes of the second- and fourth-order impulses are $A_{\pm 2} = -\frac{1}{4}(J_1(k) + J_5(k))$ and $A_{\pm 4} = \frac{1}{4}(J_1(k) - J_7(k))$, respectively. As the values of $J_5(k)$ and $J_7(k)$ in the interval of $0 \leq k \leq 3$ are almost negligible

[see Fig. 3(b)], $|A_{\pm 2}| \approx |A_{\pm 4}| \approx \frac{J_1(k)}{4}$. Therefore, both $|A_{\pm 2}|$ and $|A_{\pm 4}|$ reach their maximum values about $k = 1.8412$ [see Fig. 3(c)]; the exact values for $|A_{\pm 2}|$ and $|A_{\pm 4}|$ are $k = 1.8729$ and $k = 1.8403$, respectively (see Visualization 5).
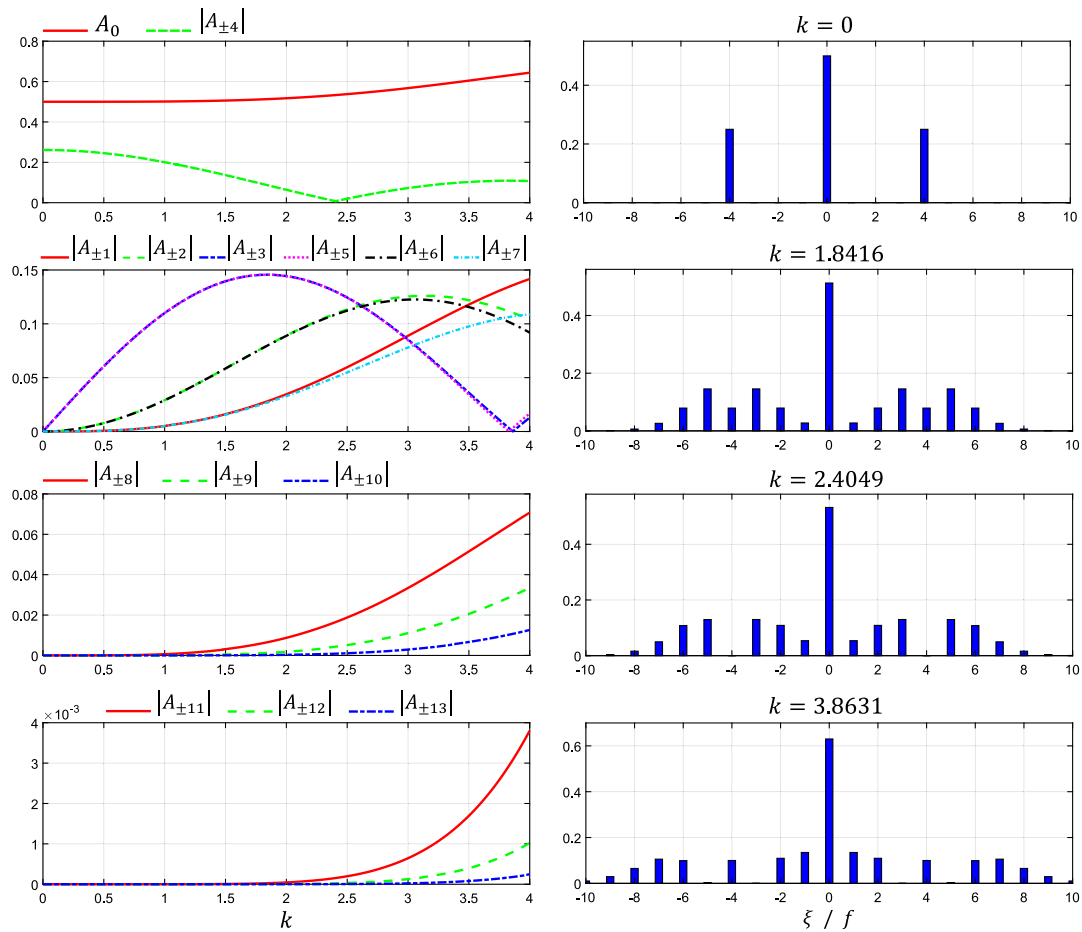
Fig. 9. Variation of different impulse amplitudes of a 1D SCASG having $n_{av} = 4$ and $n_c = 1$, in terms of k (first column). Sbsolute values of different impulse amplitudes of four gratings with different given values of FMS (second column).

The first column in Fig. 9 illustrates the variation of different impulse amplitudes of a 1D SCASG having $n_{av} = 4$ and $n_c = 1$, in terms of k. The second column depicts the impulse combs for four given values of FMS. As n_{av} is an even number, the amplitude of the DC impulse, A_0, is an ascending function of k, and its value is always more than $\frac{1}{2}$. According to Table 3 and considering $J_8(k)$ in Fig. 3, the amplitude of the fourth-order impulse is $A_{\pm n_{av}} = A_{\pm 4} = \frac{1}{4}(J_0(k) + J_8(k)) \approx \frac{J_0(k)}{4}$. As is seen in the first row of Fig. 9, $|A_{\pm 4}|$ decreases by increasing k and reaches to zero at $k = 2.4049$, which is very close to the first zero of $J_0(k)$, $k = 2.4048$. The variations of the third- and fifth-order impulses are similar. The amplitudes of the third- and fifth-order impulses are $A_{\pm 3} = -\frac{1}{4}(J_1(k) + J_7(k))$ and $A_{\pm 5} = \frac{1}{4}(J_1(k) - J_9(k))$, respectively. As the values of $J_7(k)$ and $J_9(k)$ in the interval of $0 \leq k \leq 4$ are almost negligible [see Fig. 3(b)], $|A_{\pm 3}| \approx |A_{\pm 5}| \approx \frac{J_1(k)}{4}$. Therefore, both $|A_{\pm 3}|$ and $|A_{\pm 5}|$ reach their maximum values about $k = 1.8412$ [see Fig. 3(c)]; the exact values for $|A_{\pm 3}|$ and $|A_{\pm 5}|$ are $k = 1.8416$ and $k = 1.8416$, respectively. In addition, the third- and fifth-order impulses vanish at the vicinity of $k = 3.8317$, first zero of $J_1(k)$. The exact values for $|A_{\pm 3}|$ and $|A_{\pm 5}|$ are $k = 3.8631$ and $k = 3.8319$, respectively. In a similar way, $|A_{\pm 2}| \approx |A_{\pm 6}| \approx \frac{J_2(k)}{4}$. Therefore, both the second and sixth

orders reach their maximum values about $k = 3.0542$, first maximum of $J_2(k)$ [see Fig. 3(c)].

The first column of Fig. 10 illustrates the variation of different impulse amplitudes of a 1D SCASG having $n_{av} = 5$ and $n_c = 1$, in terms of k. The second column shows the impulse combs for five different values of FMS. As n_{av} is an odd number, the amplitude of the DC impulse, A_0, is a descending function of k, and its value is always less than $\frac{1}{2}$. According to Table 4, the amplitude of the fifth-order impulse is $A_{\pm n_{av}} = A_{\pm 5} = \frac{1}{4}(J_0(k) + J_{10}(k))$. As is seen in the first row of Fig. 10, $|A_{\pm 5}|$ decreases by increasing k and reaches to zero at $k = 2.4047$, which is very close to the first zero of $J_0(k)$, $k = 2.4048$. The variations of the fourth- and sixth-order impulses are similar. The amplitudes of the fourth- and sixth-order impulses are $A_{\pm 4} = -\frac{1}{4}(J_1(k) + J_9(k))$ and $A_{\pm 6} = \frac{1}{4}(J_1(k) - J_{11}(k))$, respectively. As the values of $J_9(k)$
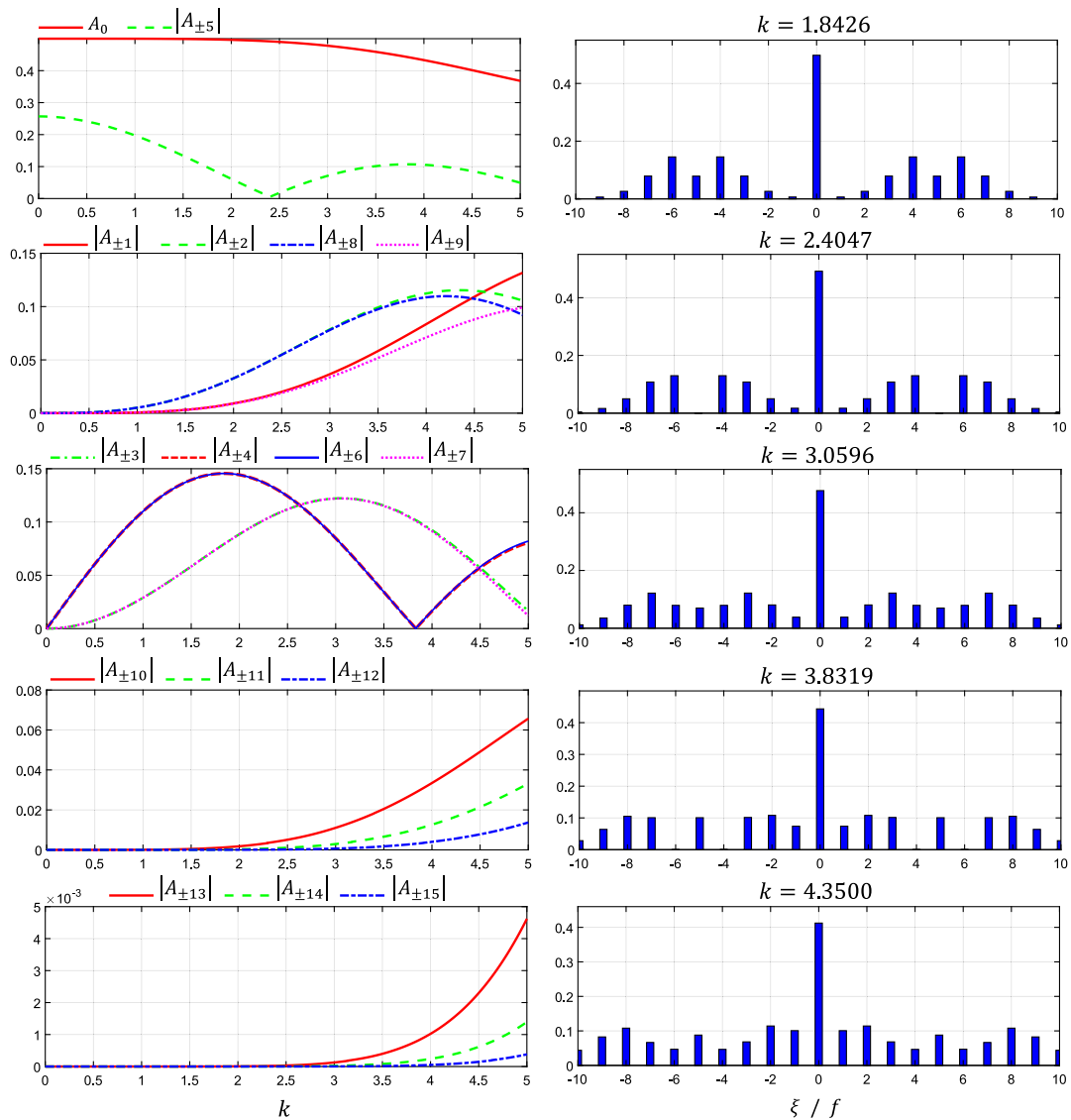
Table 3. Values of *r* and *s* Determining Amplitudes of Different Order Impulses for a 1D SCASG Having $n_{av} = 4$ and $n_c = 1$

l	± 1	± 2	± 3	± 4	± 5	± 6	± 7	± 8	± 9	± 10
r	−3	2	−1	0	1	2	3	4	5	6
s	−5	6	−7	8	−9	10	−11	12	−13	14

Fig. 10. Variation of different impulse amplitudes of a 1D SCASG having $n_{av} = 5$ and $n_c = 1$, in terms of k (first column). Absolute values of different impulse amplitudes of five gratings with different given values of FMS (second column); see Visualization 6.

and $J_{11}(k)$ in the interval of $0 \leq k \leq 5$ are almost negligible, $|A_{\pm4}| \approx |A_{\pm6}| \approx \frac{J_1(k)}{4}$. Therefore, both $|A_{\pm4}|$ and $|A_{\pm6}|$ reach their maximum values about $k = 1.8412$ [see Fig. 3(c)]; the exact values for both $|A_{\pm4}|$ and $|A_{\pm6}|$ are $k = 1.8426$. In addition, the fourth- and sixth-order impulses vanish at the vicinity of $k = 3.8317$, first zero of $J_1(k)$, and the exact values for both $|A_{\pm4}|$ and $|A_{\pm6}|$ are $k = 3.8319$. In a similar way, $|A_{\pm3}| \approx |A_{\pm7}| \approx \frac{J_2(k)}{4}$. Therefore, both the third and seventh orders reach their maximum values about $k = 3.0542$, first maximum of $J_2(k)$ [see Fig. 3(c)], and the exact values for $|A_{\pm3}|$ and $|A_{\pm7}|$ are $k = 3.0596$ and $k = 3.0547$, respectively. For the second-order impulse, its value increases by increasing k and reaches the maximum value at $k = 4.3500$, then decreases (see Visualization 6).

The first column in Fig. 11 illustrates the variation of amplitudes of some impulses in the spectrum of a 1D SCASG having $n_{av} = 7$ and $n_c = 2$, in terms of k. The second column shows

Table 4. Values of *r* and *s* Determining Amplitudes of Different Order Impulses for a 1D SCASG Having $n_{av} = 5$ and $n_c = 1$

l	±1	±2	±3	±4	±5	±6	±7	±8	±9	±10
r	4	-3	2	-1	0	1	2	3	4	5
s	6	-7	8	-9	10	-11	12	-13	14	-15

the impulse combs for three different values of FMS. According to Eq. (23), the amplitude of the DC impulse $A_0 = \frac{1}{2}$. The amplitude of the seventh-order impulse $A_{\pm n_{av}} = A_{\pm7}$ (see first row) decreases by increasing k and reaches zero at $k = 2.4052$, then increases. According to Table 2, $A_{\pm7} = \frac{1}{4}(J_0(k) - J_7(k))$. As the values of $J_7(k)$ in the interval of $0 \leq k \leq 3.5$ are almost negligible (see Fig. 3), then $A_{\pm7} \approx \frac{J_0(k)}{4}$. To determine the accuracy of this approximation, compare the first zero of $J_0(k)$, $k = 2.4048$ with the root of A_0, $k = 2.4052$. The variations of the fifth- and ninth-order impulses are similar.
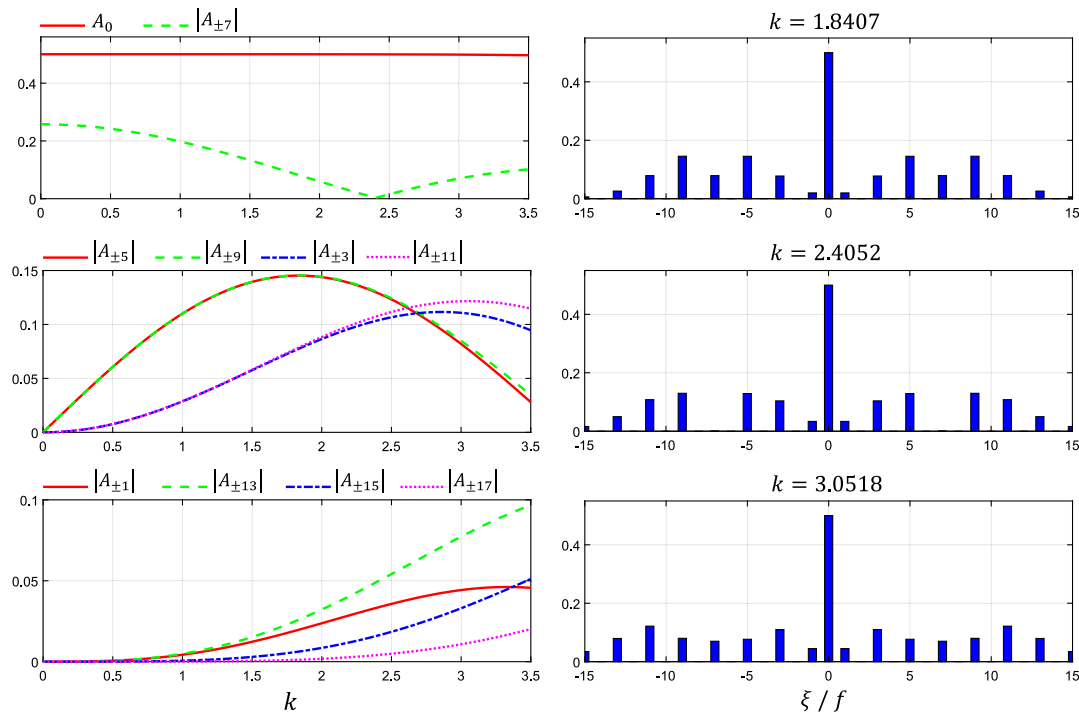
Fig. 11. Variation of different impulse amplitudes of a 1D SCASG having $n_{av} = 7$ and $n_c = 2$, in terms of k (first column). Absolute values of different impulse amplitudes of three gratings with different given values of FMS (second column).

The amplitudes of the fifth- and ninth-order impulses are $A_{\pm5} = -\frac{1}{4}(J_1(k) - J_6(k))$ and $A_{\pm9} = \frac{1}{4}(J_1(k) + J_8(k))$, respectively. As the values of $J_6(k)$ and $J_8(k)$ in the interval of $0 \le k \le 3.5$ are almost negligible, $|A_{\pm5}| \approx |A_{\pm9}| \approx \frac{J_1(k)}{4}$. Therefore, both $|A_{\pm5}|$ and $|A_{\pm9}|$ reach their maximum values about $k = 1.8412$ [see Fig. 3(c)]; the exact values for $|A_{\pm5}|$ and $|A_{\pm9}|$ are $k = 1.8372$ and $k = 1.8407$, respectively. In a similar way, $|A_{\pm3}| \approx |A_{\pm11}| \approx \frac{J_2(k)}{4}$. Therefore, both the third and eleventh orders reach their maximum values about $k = 3.0542$, first maximum of $J_2(k)$ [see Fig. 3(c)], and the exact values for $|A_{\pm3}|$ and $|A_{\pm11}|$ are $k = 2.8602$ and $k = 3.0518$, respectively.

B. Near-Field Diffraction from 1D SCASGs

Here, using the so-called angular (spatial) spectrum method [60,63,68], near-field diffraction of a plane wave from a 1D SCASG is investigated. By illuminating such a grating with a coherent uniform light beam, according to Eq. (20), light field distribution just after the grating can be written by

$$u_0(x) = \frac{1}{2}\left[1 + \sum_{m=-\infty}^{+\infty} J_m(k) \cos\left(\frac{2\pi l x}{p}\right)\right], \quad (25)$$

where $f = \frac{1}{p}$, and we suppose that the condition of periodicity of the grating is fulfilled. Then in Eq. (19), we replace $f_m = f_{av} + m f_c$ by $f_m = l f$, in which f is the fundamental frequency of the grating and $l = n_{av} + m n_c$. According to Eq. (21), the spatial spectrum of the light field just after the grating can be written as follows:

$$U_0(\xi) = \frac{1}{4}\left\{ 2\delta(\xi) + \sum_{m=-\infty}^{+\infty} J_m(k)[\delta(\xi - l f) + \delta(\xi + l f)]\right\}. \quad (26)$$

In Fresnel approximation, by multiplying this expression to the free space transfer function,

$$H = H_0 \exp[-i\pi\lambda z \xi^2], \quad (27)$$

the spatial spectrum at a distance z from the grating is obtained in the following form:

$$U_z(\xi) = \frac{1}{2}\delta(\xi) + \frac{1}{4}\left\{ \sum_{m=-\infty}^{+\infty} J_m(k)e^{-i\pi\lambda z \xi^2} \right.$$
$$\left. \times [\delta(\xi - l f) + \delta(\xi + l f)]\right\}, \quad (28)$$

where $H_0 = \exp(ikz)$ is ignored for simplicity. The field distribution at a distance z from the grating can be calculated by taking the inverse Fourier transform from Eq. (27),

$$u_z(x) = \frac{1}{2} + \frac{1}{4}\left\{ \sum_{m=-\infty}^{+\infty} J_m(k)e^{-i\pi\lambda z(l f)^2}[e^{i2\pi l f x} + e^{-i2\pi l f x}]\right\}. \quad (29)$$

By defining $z_T = \frac{2}{\lambda f^2} = \frac{2p^2}{\lambda}$ as Talbot distance of the grating, the resulting diffraction pattern can be rewritten in the following form:
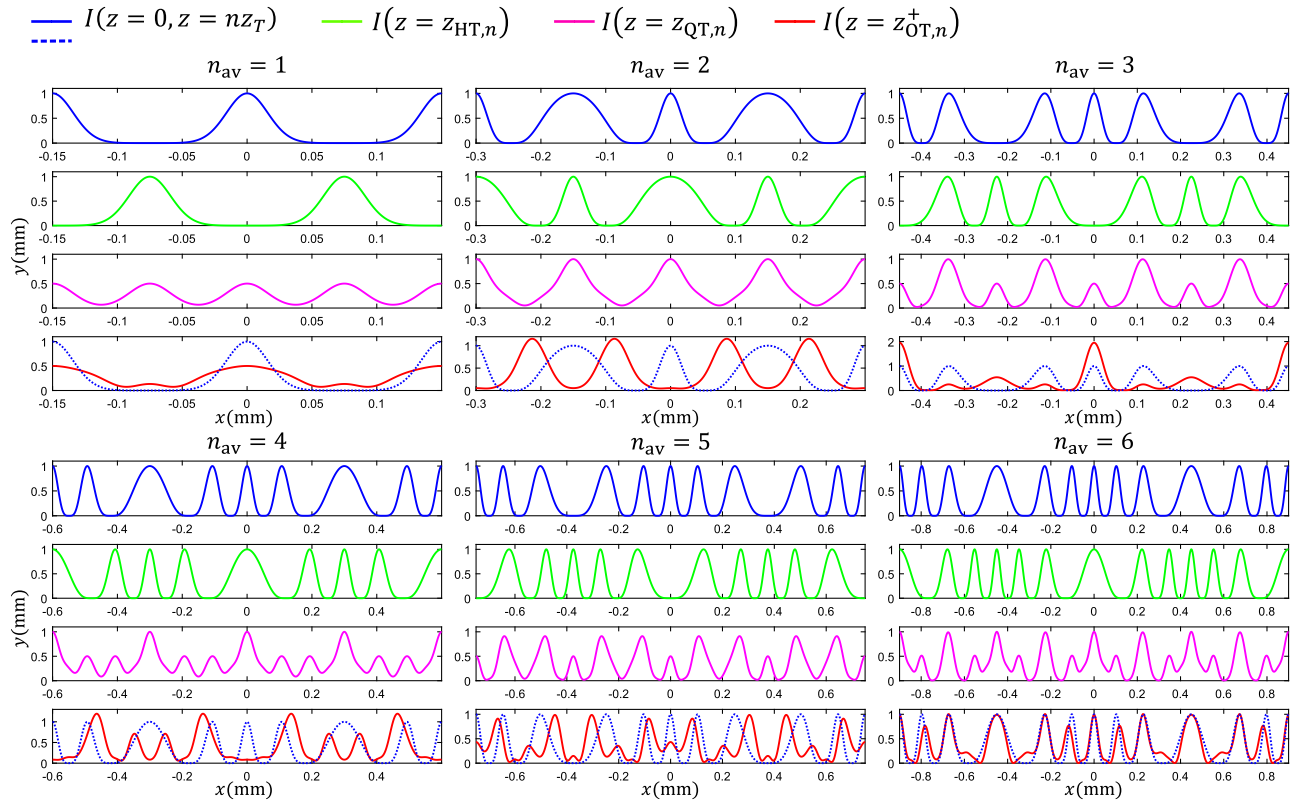
Fig. 12. Intensity profiles of the diffracted light from the gratings illustrated in the first column of Fig. 1, just after the grating and at the Talbot (first and fifth rows), half-Talbot (second and sixth rows), quarter-Talbot (third and seventh rows), and octant-Talbot (fourth and eighth rows) distances; see Visualization 7, Visualization 8, Visualization 9, and Visualization 10.

$$u_z(x) = \frac{1}{2}\left[1 + \sum_{m=-\infty}^{+\infty} J_m(k) e^{-i2\pi l^2 \frac{z}{z_T}} \cos\left(\frac{2\pi l x}{p}\right)\right].$$

(30)

Comparing Eqs. (24) and (29), we see that, when the propagation distance z equals to an integer multiple of z_T, the light amplitude exactly recovers its initial form. Figures 12 and 13 illustrate the intensity profiles of the diffracted light from the gratings shown in the first and second columns of Fig. 1, immediately after the grating and at different distances from the gratings. As is apparent, at Talbot distances, the light field completely recovers its initial shape.

In so-called half-Talbot distances $z_{\mathrm{HT},n} = (2n-1)\frac{z_T}{2}$, $n = 1, 2, 3, \ldots$, using Eq. (29), we have

$$u_{z=z_{\mathrm{HT},n}}(x) = \frac{1}{2}\left[1 + \sum_{m=-\infty}^{+\infty} J_m(k)(-1)^l \cos\left(\frac{2\pi l x}{p}\right)\right],$$

(31)

where we used $\exp[-i(2n-1)\pi] = -1$ and $(-1)^{l^2} = (-1)^l$. Now using $\cos(\theta - l\pi) = (-1)^l \cos(\theta)$, Eq. (30) reduces to

$$u_{z=z_{\mathrm{HT},n}}(x) = \frac{1}{2}\left\{1 + \sum_{m=-\infty}^{+\infty} J_m(k) \cos\left[\frac{2\pi l}{p}\left(x - \frac{p}{2}\right)\right]\right\}.$$

(32)

Comparing Eqs. (31) and (24), one can deduce that

$$u_{z=z_{\mathrm{HT},n}}(x) = u_0\left(x - \frac{p}{2}\right),$$

(33)

which means that at the half-Talbot distances the amplitude fully recovers its initial form but with a lateral half-period shift, comparing the first and second rows, and the fifth and the sixth rows, in Figs. 12 and 13. This is a well-known feature of the Talbot effect.

Let us now investigate quarter-Talbot distances, $z_{\mathrm{QT},n} = (2n-1)\frac{z_T}{4}$, namely the halfway between the Talbot planes and their nearest half-Talbot planes. Substituting $z = z_{\mathrm{QT},n}$ in Eq. (29), we get

$$u_{z=z_{\mathrm{QT},n}}(x) = \frac{1}{2}\left[1 + \sum_{m=-\infty}^{+\infty} J_m(k)(-1)^{nl^2}(i)^{l^2} \cos\left(\frac{2\pi l x}{p}\right)\right].$$

(34)

Details of derivation are similar to the derivation of Eq. (22) of [61], when l gets even values $(-1)^{nl^2}(i)^{l^2} = 1$ and when l gets odd values $(-1)^{nl^2}(i)^{l^2} = i(-1)^n$ [61]. As the value of l depends on the values of n_c and n_{av}, three different possible cases (groups) are as follows: both n_c and n_{av} are odd numbers (first case), n_c is odd and n_{av} is even (second case), and n_c is even and n_{av} is odd (third case). In the first case, if m is even (odd), then the value of l is odd (even). In the second case, if m is even (odd), then the value of l is even (odd). In the third case, l is always odd regardless of the value of m. Therefore, in the first and second cases, Eq. (33) reduces to
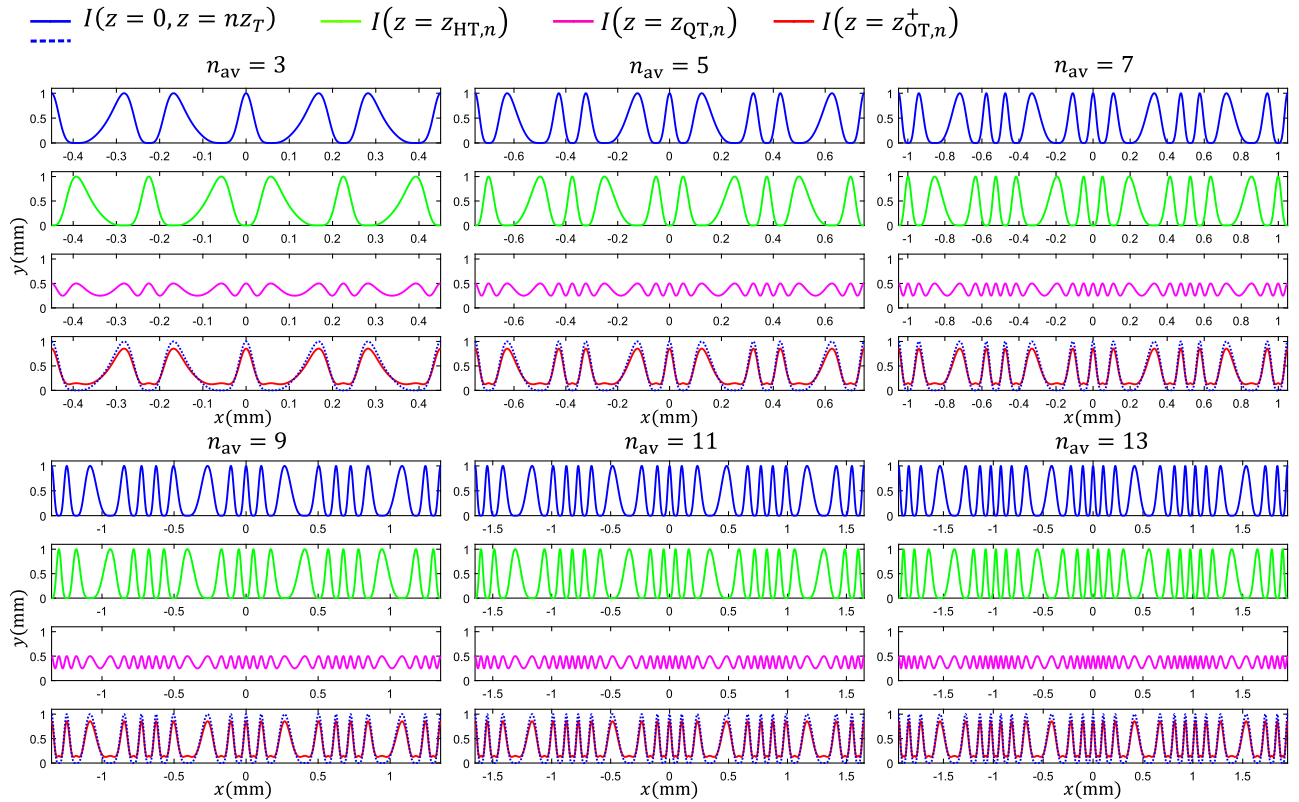
Fig. 13. Intensity profiles of the diffracted light from the gratings illustrated in the second column of Fig. 1, just after the grating and at the Talbot (first and fifth rows), half-Talbot (second and sixth rows), quarter-Talbot (third and seventh rows), and octant-Talbot (fourth and eighth rows) distances; see Visualization 11, Visualization 12, Visualization 13, and Visualization 14.

$$u_{z=z_{\mathrm{QT},n}}(x) = \frac{1}{2}\left[1 + \sum_{\substack{m=-\infty \\ \mathrm{odd}}}^{+\infty} J_m(k)\cos\left(\frac{2\pi lx}{p}\right) \right.$$

$$\left. \times +i(-1)^n \sum_{\substack{m=-\infty \\ \mathrm{even}}}^{+\infty} J_m(k)\cos\left(\frac{2\pi lx}{p}\right) \right], \tag{35}$$

$$u_{z=z_{\mathrm{QT},n}}(x) = \frac{1}{2}\left[1 + \sum_{\substack{m=-\infty \\ \mathrm{even}}}^{+\infty} J_m(k)\cos\left(\frac{2\pi lx}{p}\right) \right.$$

$$\left. \times +i(-1)^n \sum_{\substack{m=-\infty \\ \mathrm{odd}}}^{+\infty} J_m(k)\cos\left(\frac{2\pi lx}{p}\right) \right], \tag{36}$$

respectively. As is apparent, real and imaginary parts of the complex amplitude are separated for both cases. Therefore, their complex amplitudes can be rewritten in the following form:

$$u_{z=z_{\mathrm{QT},n}}(x) = u_r(x) + iu_i(x), \tag{37}$$

where $u_r(x)$ and $u_i(x)$ are two real and periodic functions with periods $\frac{p}{2}$ and p, respectively. As the Fourier expansion of $u_i(x)$ includes only odd values of l, the fundamental period of $u_i(x)$

halves by squaring, while the fundamental period of $u_r(x)$ does not change by squaring. Therefore, the fundamental period of the intensity profile at quarter-Talbot distances,

$$I_{z=z_{\mathrm{QT},n}}(x) = u_r(x)^2 + u_i(x)^2, \tag{38}$$

is $\frac{p}{2}$. The details can be obtained using the theory presented in the second and third sections of [61]. This attribute is also well-known in the Talbot effect. According to the main result of [61], and as for the first and second cases, the Fourier expansion of the gratings, Eq. (24), includes both even and odd values of l, and the contrast of the quarter-Talbot sub-images must have considerable values. This feature is obviously seen in Fig. 12 (see the third and seventh rows). Moreover, comparing Eqs. (34) and (35) with Eq. (24), we deduce that quarter-Talbot sub-images must lose their similarity with the initial ($z = 0$) intensity profile. This feature is also apparently seen in Fig. 12, comparing the first and third rows, and the fifth and the seventh rows.

In the third case, Eq. (33) reduces to

$$u_{z=z_{\mathrm{QT},n}}(x) = \frac{1}{2}\left[1 + i(-1)^n \sum_{m=-\infty}^{+\infty} J_m(k)\cos\left(\frac{2\pi lx}{p}\right) \right]. \tag{39}$$

In this case again by considering Eq. (38) in the form of Eq. (36), it can be shown that the fundamental period of the intensity profile at quarter-Talbot distances is $\frac{p}{2}$. As the Fourier expansion of the grating, Eq. (24), includes only odd values of l, the quarter-Talbot sub-images must not have considerable contrasts, again
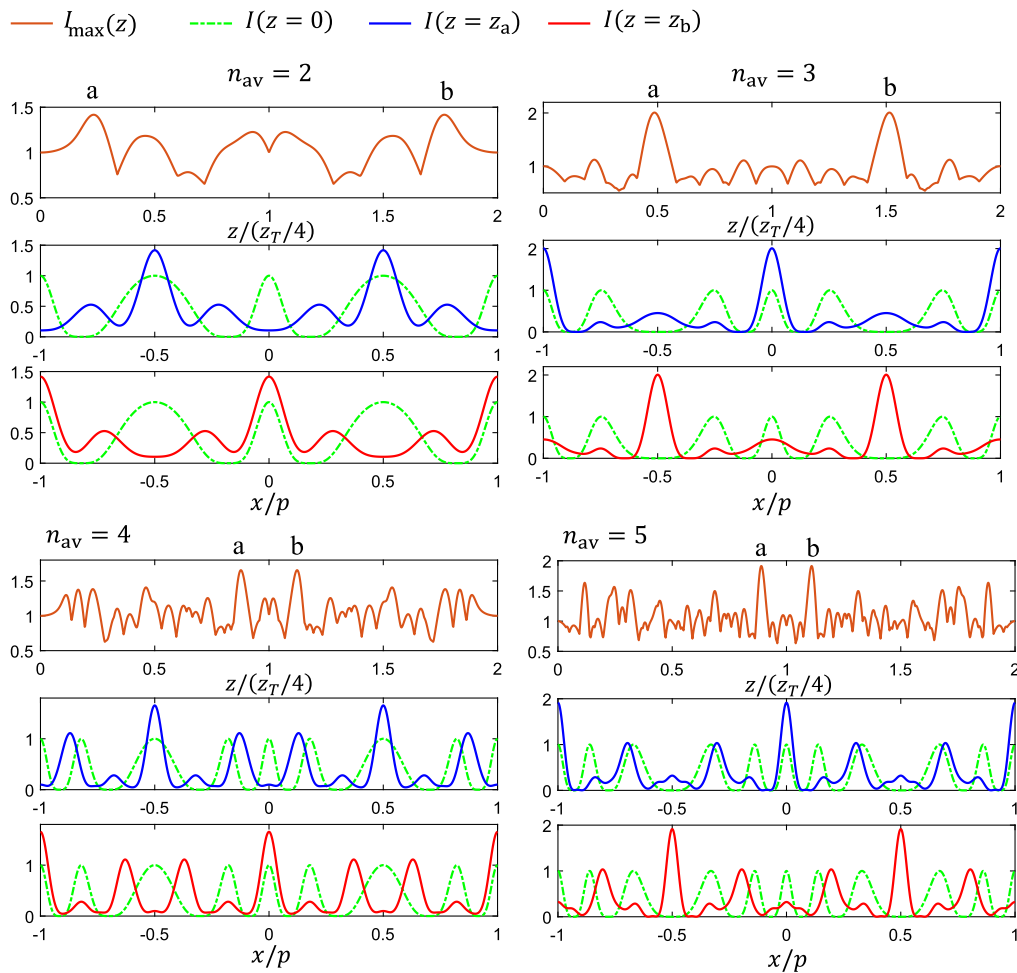
Fig. 14. First and fourth rows, plots of the maximum intensity detected over the diffraction patterns for the gratings illustrated in the first column of Fig. 1, in terms of the propagation distance. Second, third, fifth, and sixth rows, corresponding intensity profiles just after the gratings (dashed green curves) and at the distances in which the $I_{\max}(z)$ is absolute maximum (solid blue and red curves).

according to the results of [61]. Moreover, comparing Eqs. (38) and (24), we deduce that quarter-Talbot sub-images must maintain their similarity with the initial ($z = 0$) intensity profile. This feature is also apparently seen in Fig. 13, comparing the first and third rows, and the fifth and the seventh rows.

Now let us consider near-field diffraction patterns at octant-Talbot distances $z_{\mathrm{OT,n}}^{\pm} = (n \pm \frac{1}{4}) \frac{z_T}{2}$, where $n = 1, 2, 3, \ldots$. By substituting $z = z_{\mathrm{OT,n}}^{\pm}$ in Eq. (29), we get

$$u_{z=z_{\mathrm{OT,n}}^{\pm}}(x) = \frac{1}{2}\left[1 + \sum_{m=-\infty}^{+\infty} J_m(k)(-1)^{nl}(\mp i)^{l^2/2} \cos\left(\frac{2\pi lx}{p}\right) \right]. \tag{40}$$

It can be shown that

$$(-1)^{nl}(\mp i)^{l^2/2} = \begin{cases} i^l, & \text{if } l \text{ is even,} \\ (-1)^n \sqrt{\mp i}, & \text{if } l \text{ is odd.} \end{cases} \tag{41}$$

See Appendix A of [61]. Therefore, in the first to third cases, Eq. (39) reduces to

$$u_{z=z_{\mathrm{OT,n}}^{\pm}}(x) = \frac{1}{2}\left[1 + \sum_{\substack{m=-\infty \\ \text{odd}}}^{+\infty} i^l J_m(k) \cos\left(\frac{2\pi lx}{p}\right) \right.$$
$$\left. \times + (-1)^n \sqrt{\mp i} \sum_{\substack{m=-\infty \\ \text{even}}}^{+\infty} J_m(k) \cos\left(\frac{2\pi lx}{p}\right) \right], \tag{42}$$

$$u_{z=z_{\mathrm{OT,n}}^{\pm}}(x) = \frac{1}{2}\left[1 + \sum_{\substack{m=-\infty \\ \text{even}}}^{+\infty} i^l J_m(k) \cos\left(\frac{2\pi lx}{p}\right) \right.$$
$$\left. \times + (-1)^n \sqrt{\mp i} \sum_{\substack{m=-\infty \\ \text{odd}}}^{+\infty} J_m(k) \cos\left(\frac{2\pi lx}{p}\right) \right], \tag{43}$$

$$u_{z=z_{\mathrm{OT,n}}^{\pm}}(x) = \frac{1}{2}\left[1 + (-1)^n \sqrt{\mp i} \sum_{m=-\infty}^{+\infty} J_m(k) \cos\left(\frac{2\pi lx}{p}\right) \right], \tag{44}$$
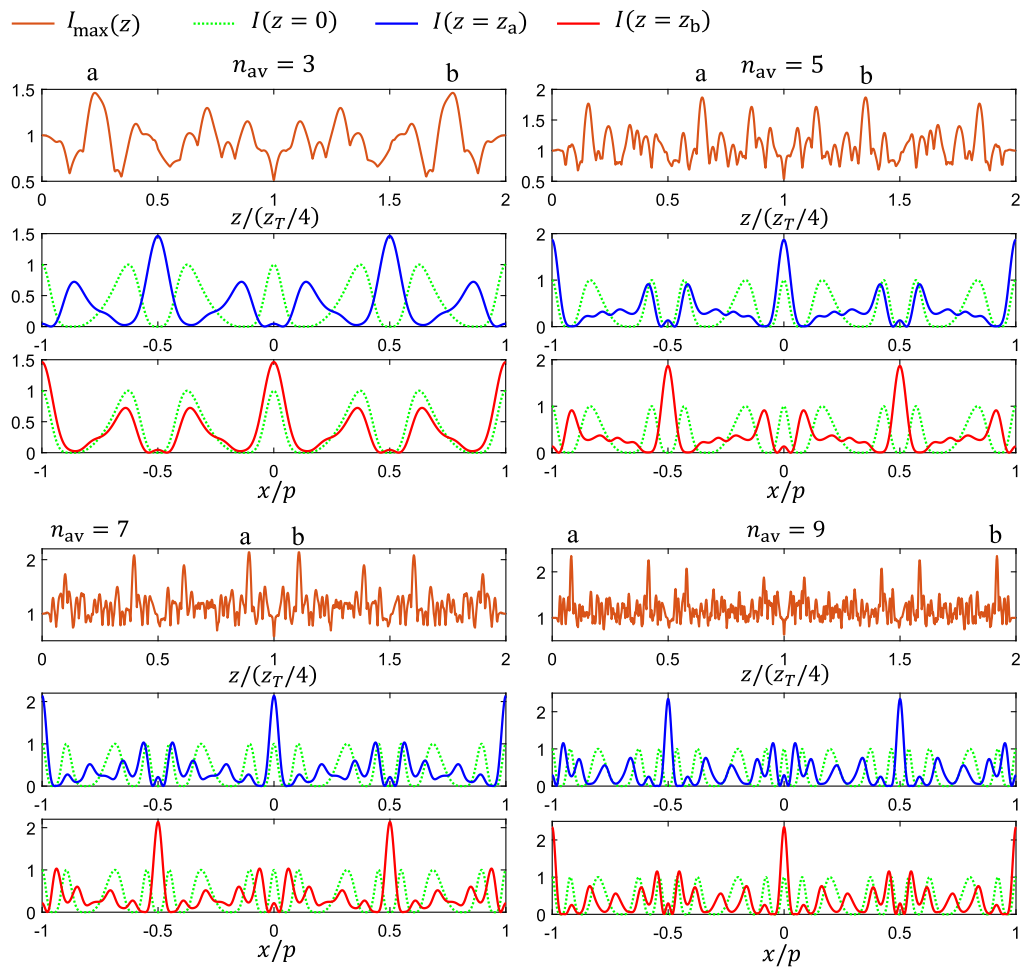
Fig. 15.   The same plots as in Fig. 14 are calculated for the gratings illustrated in the second column of Fig. 1.
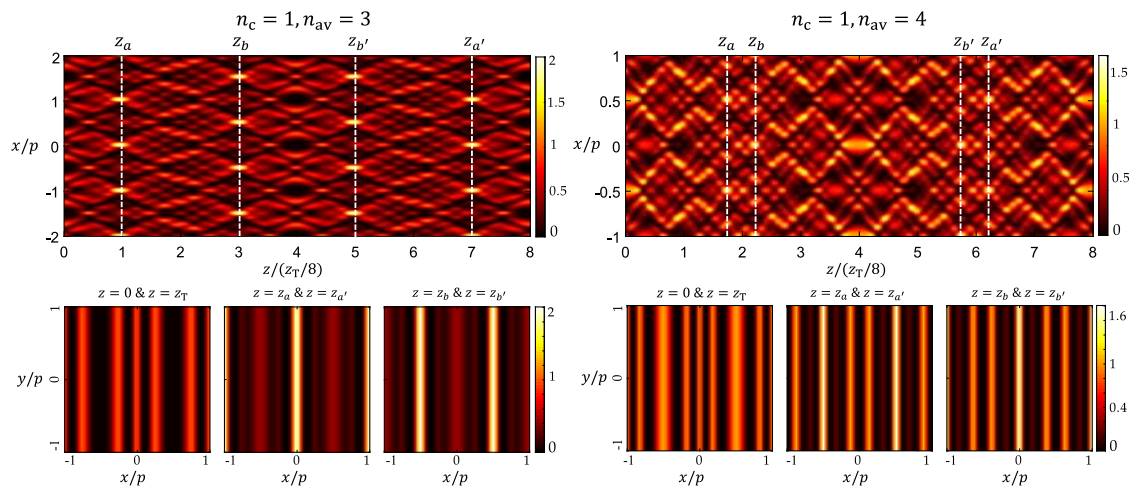

Fig. 16.   First row, Talbot carpets of two gratings from Fig. 1. Second row, intensity patterns immediately after the grating and at the Talbot distance, and four distances at which $I_{max}(z)$ is maximum. Colorbars are normalized to the intensity of the incident beam (see Visualization 15, Visualization 16, Visualization 17, and Visualization 18).

respectively. Comparing the last three equations with Eq. (24), we expect that only in the third case the intensity profile of the produced Fresnel images is very similar to the initial ($z = 0$) profile. This fact is obviously shown in the fourth and eighth rows of

Figs. 12 and 13. A similar behavior at octant-Talbot planes of the Ronchi grating was reported by Patorski *et al.* in 1982 [69].

In the background Visualization 7, Visualization 8, Visualization 9, Visualization 10, Visualization 11,
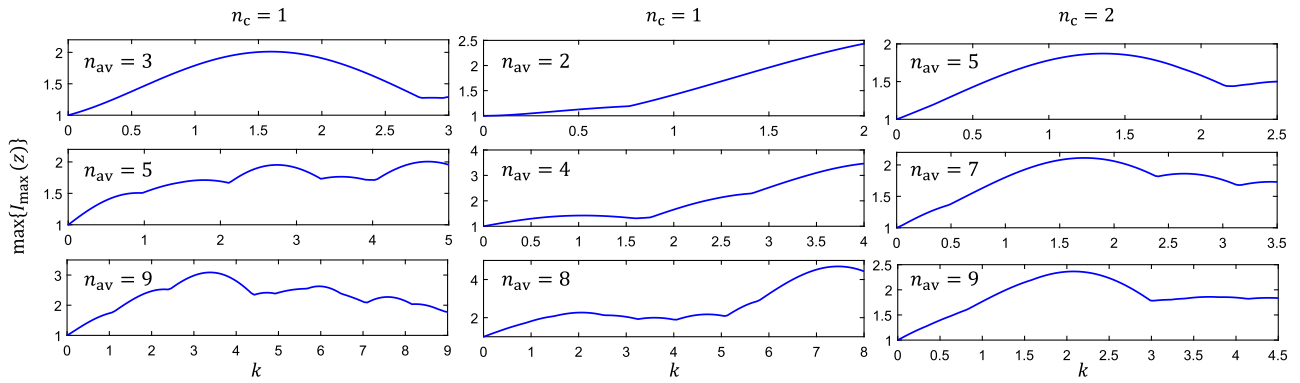
Fig. 17. Variation of the parameter $\max\{I_{\max}(z)\}$ in terms of FMS for the gratings having different values of n_c and n_{av}.
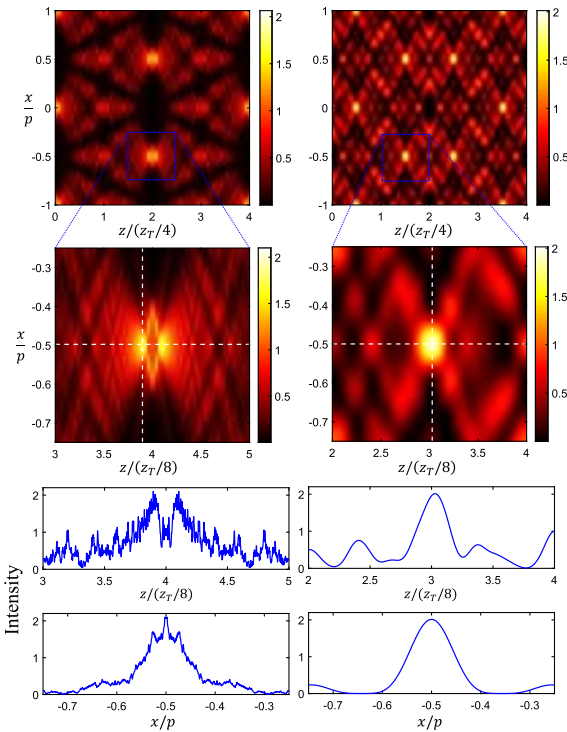

Fig. 18. First row, Talbot carpets of a binary grating with $\mu = 0.25$ (first column) and a 1D SCASG with $n_c = 1$, $n_{av} = 3$, and $k = 1.6$ (second column). Second row, corresponding high resolution insets including one of the bright spots over the Talbot carpets. Third and fourth rows, intensity profiles along the white lines shown over the insets.

Visualization 12, Visualization 13, and Visualization 14, evolutions of 1D profiles of the diffracted light fields from different 1D SCASGs under propagation are presented. Some interesting aspects can be seen in these visualizations. For instance, in some propagation distances, the intensity profiles possess sharp and smooth peaks having maximum intensities greater than the intensity of the incident light beam. It is noteworthy that, also in the diffraction of a plane wave from a binary grating, there are some non-smooth bright areas over the corresponding Talbot carpet at the vicinity of the Talbot distances (before and after). We will come back to this issue and present the details of the differences between the bright spots over the
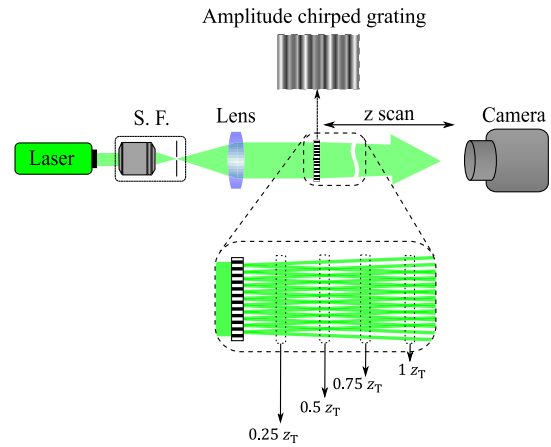

Fig. 19. Schematic diagram of the experimental setup.

Talbot carpets of binary gratings and 1D SCASGs. By plotting the maximum intensity of the diffraction patterns in terms of the propagation distance, $I_{\max}(z)$, one can find the distances at which the $I_{\max}(z)$ are the absolute maximum. The first and fourth rows of Figs. 14 and 15 show the maximum intensity over the diffraction patterns, $I_{\max}(z)$, under propagation from $z = 0$ to $z = z_T/2$, for the gratings illustrated in the first column of Fig. 1. In two propagation distances, illustrated by the letters a and b on the plots, the value of $I_{\max}(z)$ reaches its maximum. Intensity profiles at $z = z_a$ and $z = z_b$ are depicted in the second, third, fifth, and sixth rows. As is seen, the maximum value of $I_{\max}(z)$ depends on the value of n_c and n_{av}.

For getting full information about the diffraction pattern changes along z axis, in Fig. 16 the Talbot carpets of two different gratings of Fig. 1 are depicted. As is expected, the maximum intensity of the Talbot carpets is more than the intensity of incident beam (see colorbars). In other words, there exist some bright spots over the carpets where the intensity is higher than the incident beam's intensity. In fact, these bright spots are the cross section of intensity bars formed over the transverse plans at $z = z_a$ and $z = z_b$ distances. The intensity of these bright bars, $\max\{I_{\max}(z)\}$, depends on the parameters of the gratings. In Visualization 15, Visualization 16, Visualization 17, and Visualization 18, by changing FMS of the gratings (with definite values of n_c and n_{av}) from $k = 0$ to $k = \frac{n_{av}}{n_c}$, one can chase the variation of the parameter $\max\{I_{\max}(z)\}$. By the aid of
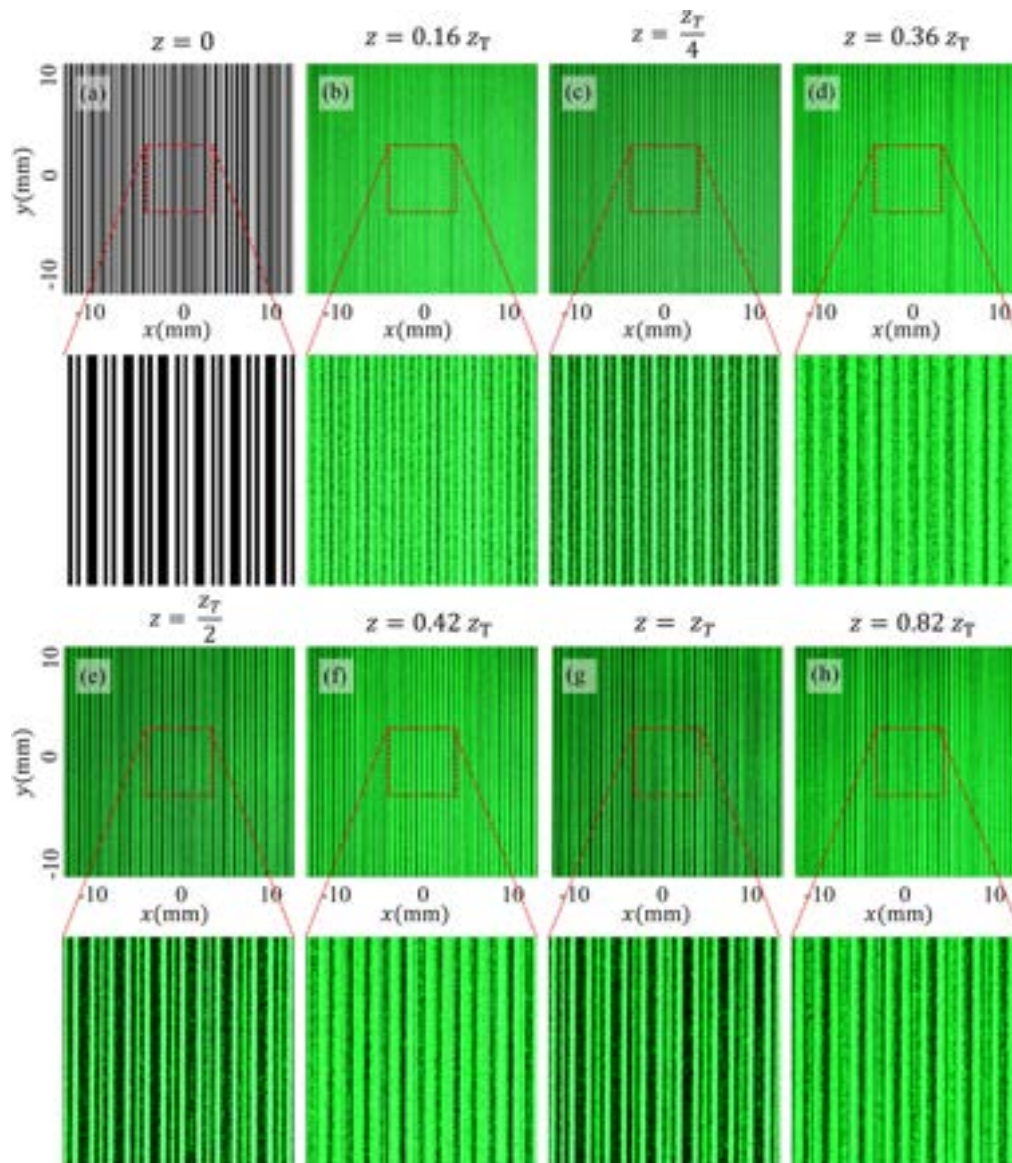
Fig. 20. Near-field intensity patterns of a 1D spatially chirped amplitude binary grating with $p_1 = 0.1$ mm, $p_2 = 0.3$ mm, $p_c = 0.45$ mm, $n_c = 1$, and $n_{av} = 3$ at different propagation distances: (a) immediately after the grating, (c) at the quarter-Talbot distance $z = \frac{z_T}{4}$, (e) at the half-Talbot distance $z = \frac{z_T}{2}$, and (g) at the Talbot distance $z = z_T$; the others are not Talbot distance.

this approach, the intensity of the brightest spot over the Talbot carpet is depicted in terms of FMS for the gratings having different values of n_c and n_{av} in Fig. 17. As is apparent, by choosing appropriate values for n_c, n_{av}, and FMS of a 1D SCASG, the value of max{$I_{max}(z)$} reaches to several times of the intensity of the incident beam. This feature might find applications for trapping and aggregation of particles along straight lines.

It is worth noting that, in the diffraction of a plane wave from a binary grating, the corresponding Talbot carpet also includes bright spots having intensities higher than the intensity of the incident beam. To show the advantages of the proposed gratings, in Fig. 18 we present Talbot carpets of a binary grating and a 1D SCASG. The parameters of the gratings are chosen so that the maximum intensities of the Talbot carpets are almost equal. To illustrate the differences between the intensity distribution around the bright spots, high resolution insets of the Talbot carpets are presented in the second row. The next rows show

1D intensity profiles passing through the points having maximum intensities in the propagation and transverse directions. By looking at the second to the last row, it is apparent that the bright spot of the binary grating splits into two closed spots with non-smooth profiles, while the bright spot of the 1D SCASG is isolated and has completely smooth profiles. It should be noted that in [42], by considering a certain randomness for the opening ratio of a binary grating, they smoothed the resulting Talbot carpet. As a result of smoothing, the maximum intensity of bright spots and the contrast of self-images remarkably decrease (see Fig. 2 of [42]).

5. EXPERIMENTS

In the experiments, we used the second harmonic of an Nd:YAG diode-pumped laser beam having a wavelength of $\lambda = 532$ nm,
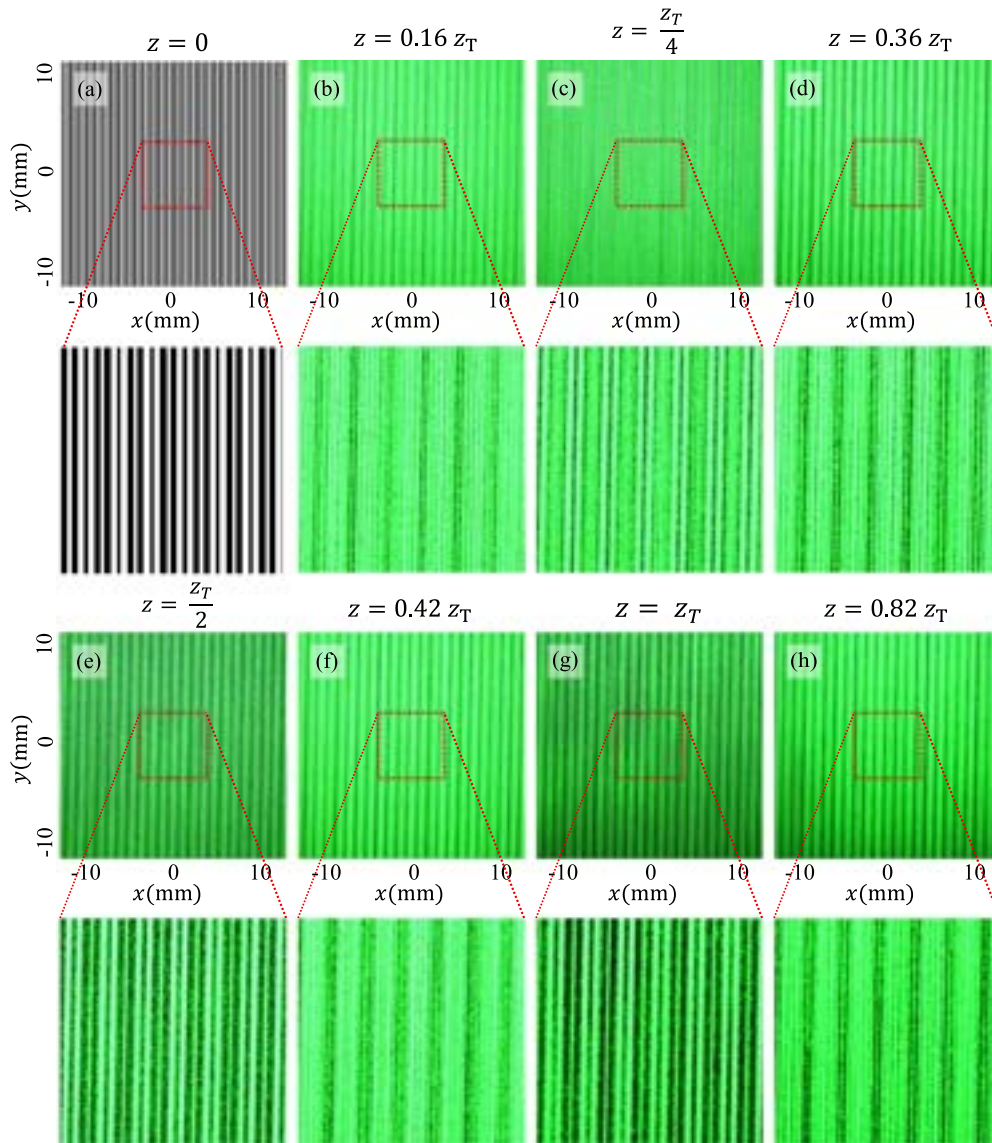
Fig. 21.   Near-field intensity patterns of a 1D spatially chirped amplitude binary grating with $p_1 = 0.1$ mm, $p_2 = 0.3$ mm, $p_c = 0.225$ mm, $n_c = 2$, and $n_{av} = 3$ at different propagation distances: (a) immediately after the grating, (c) at the quarter-Talbot distance $z = \frac{z_T}{4}$, (e) at the half-Talbot distance $z = \frac{z_T}{2}$, and (g) at the Talbot distance $z = z_T$; the others are not Talbot distance.

which was spatially filtered and collimated, respectively, using a spatial filter and a doublet lens (see Fig. 19).

Since we produced the needed gratings simply by printing their transmission functions on the transparency sheets, and due to the low spatial resolution of the used printers, we were forced to print binary gratings instead of a sinusoidal one on the sheet plates. As 1D spatially chirped amplitude sinusoidal and binary gratings show almost the same near-field diffraction patterns, the use of binary gratings is reasonable.

A 1D spatially chirped amplitude binary grating is placed on a holder in which the grating's plane is perpendicular to the optical axis of the beam. We use a digital camera (NIKON D7200) to record the diffraction patterns at different distances from the grating. The camera's lens is removed, and the diffracted pattern is directly imaged on its sensitive area. The dimensions of the

used gratings were 30 $mm \times 30$ mm. In the experiments, they are fully illuminated by the laser beam.

In Fig. 20, experimentally recorded near-field intensity patterns of a 1D spatially chirped amplitude binary grating with $p_1 = 0.1$ mm, $p_2 = 0.3$ mm, $p_c = 0.45$ mm, $n_c = 1$, and $n_{av} = 3$ are illustrated. The intensity patterns immediately after the grating [Fig. 20(a)], at the quarter-Talbot distance $z = \frac{z_T}{4}$ [Fig. 20(c)], at the half-Talbot distance $z = \frac{z_T}{2}$ [Fig. 20(e)], and at the Talbot distance $z = z_T$ [Fig. 20(g)] are shown. As is apparent, we have the self-image of the structures at the quarter-Talbot, at the half-Talbot, and at the Talbot distances. We also see laterally shifted self-images at the half-Talbot distances, while for the other distances, namely patterns in Figs. 20(b), 20(d), 20(f), and 20(h), which are not the Talbot distances, we do not see the self-images. Similarly, in Figs. 21 and 22, the experimentally recorded near-field intensity patterns of two
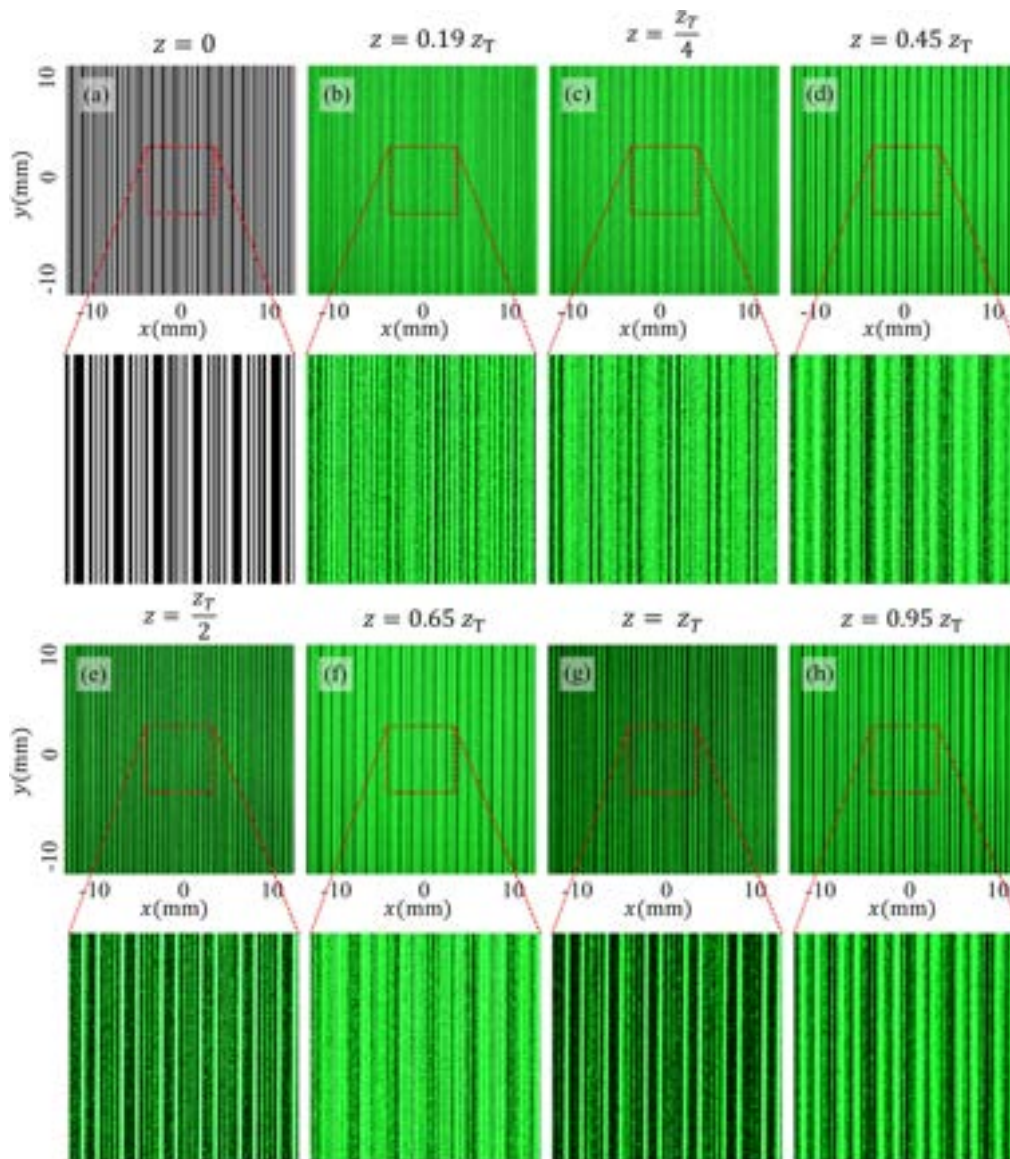
Fig. 22.   Near-field intensity patterns of a 1D spatially chirped amplitude binary grating with $p_1 = 0.06$ mm, $p_2 = 0.3$ mm, $p_c = 0.5$ mm, $n_c = 1$, and $n_{av} = 5$ at different propagation distances: (a) immediately after the grating, (c) at the quarter-Talbot distance $z = \frac{z_T}{4}$, (e) at the half-Talbot distance $z = \frac{z_T}{2}$, and (g) at the Talbot distance $z = z_T$; the others are not Talbot distance.

sets of gratings are illustrated. For the first set, $p_1 = 0.1$ mm, $p_2 = 0.3$ mm, $p_c = 0.225$ mm, $n_c = 2$, and $n_{av} = 3$, and for the second set, $p_1 = 0.06$ mm, $p_2 = 0.3$ mm, $p_c = 0.5$ mm, $n_c = 1$, and $n_{av} = 5$. Figures 21 and 22 show the intensity patterns at different distances from the gratings: immediately after the grating [Figs. 21(a) and 22(a)], at the quarter-Talbot distance $z = \frac{z_T}{4}$ [Figs. 21(c) and 22(c)], at the half-Talbot distance $z = \frac{z_T}{2}$ [Figs. 21(e) and 22(e)], and at the Talbot distance $z = z_T$ [Figs. 21(g) and 22(g)].

6. CONCLUSION

A new class of 1D spatial-frequency-modulated structures was introduced, and their spatial spectrum and near-field diffraction were investigated. Considering a sinusoidal frequency modulation, we defined 1D spatially chirped structures in which the spatial frequency sinusoidally alternates between two values, say f_1 and f_2. We showed that the transmittance of these structures is generally an almost-periodic function with an impulsive spatial spectrum. However, we found the condition under which the transmittance of these structures is a periodic function; therefore, the spatial spectrum forms a 1D lattice of impulses. Under this condition, we called them 1D spatially chirped periodic structures, and they were characterized by three parameters: n_c, n_{av}, and FMS. Based on the transmittance of a conventional amplitude sinusoidal grating, we defined a 1D SCASG and rigorously investigated its spatial spectrum. It was shown that the spatial spectrum of such grating can be managed by adjusting the characteristic values of the grating. This feature might find applications in power sharing of the incident beam among different diffraction orders. Furthermore, using the so-called angular (spatial) spectrum method, near-field

diffraction from a 1D SCASG was studied. It was also shown that the diffraction patterns at the fractional Talbot distances depend on the characteristic parameters of the grating. In some propagation distances, over the diffraction patterns, there are some sharp bright intensity bars having smooth profiles and maximum intensities equal to several times of the incident light beam's intensity. The intensity of these bright bars depends on the FMS of the grating and can be maximized by adjusting the value of FMS. These bright bars might find applications for trapping and aggregation of particles along straight lines. In the continuum of this work, the diffraction from a grating constructed by an array of 1D zone-plate-like apparatuses is under study, where this kind of structure might find applications in electromagnetic waves having long wavelengths.

APPENDIX A

Here we briefly review the definition and properties of almost-periodic functions as an important generalization of the periodic functions. Based on the Fourier theory, if $g(x)$ is a periodic function with a period p, then it can be uniquely expanded in a Fourier series:

$$g(x) = \sum_{n=-\infty}^{+\infty} A_n \exp(i2\pi n f x), \tag{A1}$$

where $f = 1/p$ is the fundamental frequency of $g(x)$ and the Fourier coefficients A_n are given by

$$A_n = \frac{1}{p} \int_p g(x) \exp(-i2\pi n f x) \mathrm{d}x, \tag{A2}$$

in which $\int_p$ indicates an integration over any arbitrary interval having a length p. Taking the Fourier transform, the spectrum of the periodic function $g(x)$ can be expressed as follows [62]:

$$G(\xi) = \sum_{n=-\infty}^{+\infty} A_n \delta(\xi - nf), \tag{A3}$$

where δ is the impulse symbol. As is apparent, the spectrum is a comb of impulses with a fixed step f whose n th impulse is located at the frequency $\xi = nf$ with an amplitude A_n.

An almost-periodic function can be uniquely expanded in the form of a generalized Fourier series [62]:

$$g(x) = \sum_{n=-\infty}^{+\infty} A_n \exp(i2\pi f_n x), \tag{A4}$$

where f_n are arbitrary real numbers, and the complex numbers A_n are called the Fourier coefficients and are given by

$$A_n = \lim_{p \to \infty} \frac{1}{p} \int_p g(x) \exp(-i2\pi f_n x) \mathrm{d}x, \tag{A5}$$

in which $\int_p$ indicates an integration over an arbitrary interval of length p. It should be noted that the infinite sum in Eq. (A4) is a generalized Fourier series, in which the frequencies f_n are no longer integer multiples of a fundamental frequency f, as was

in Eq. (A1) for a periodic function $g(x)$. The spectrum of an almost-periodic function can be written as follows:

$$G(\xi) = \sum_{n=-\infty}^{+\infty} A_n \delta(\xi - f_n). \tag{A6}$$

As is seen, the spectrum of an almost-periodic function includes a denumerable set of impulses, which are located at the frequencies f_n, and their amplitudes are A_n. Indeed, the main feature of an almost-periodic function has an impulsive spectrum, as a generalization of the spectrum of a periodic function. Although it still consists of a denumerable set of impulses, it is not limited to a comb of impulses with a fixed step, as in Eq. (A3), and it may consist of any set of impulses with arbitrary frequencies f_n.

Data availability. No data were generated or analyzed in the presented research.

REFERENCES

1. J. Wen, Y. Zhang, and M. Xiao, "The Talbot effect: recent advances in classical optics, nonlinear optics, and quantum optics," Adv. Opt. Photon. **5**, 83–130 (2013).
2. J. Cowley and A. Moodie, "Fourier images IV: the phase grating," Proc. Phys. Soc. **76**, 378–384 (1960).
3. W. D. Montgomery, "Self-imaging objects of infinite aperture," J. Opt. Soc. Am. **57**, 772–778 (1967).
4. K. Patorski, "I The self-imaging phenomenon and its applications," Prog. Opt. **27**, 1–108 (1989).
5. V. Arrizón and G. Rojo-Velázquez, "Fractional Talbot field of finite gratings: compact analytical formulation," J. Opt. Soc. Am. A **18**, 1252–1256 (2001).
6. A. W. Lohmann, H. Knuppertz, and J. Jahns, "Fractional Montgomery effect: a self-imaging phenomenon," J. Opt. Soc. Am. A **22**, 1500–1508 (2005).
7. K. Pelka, J. Graf, T. Mehringer, and J. von Zanthier, "Prime number decomposition using the Talbot effect," Opt. Express **26**, 15009–15014 (2018).
8. K. Patorski and G. Parfjanowicz, "Self-imaging phenomenon of a sinusoidal complex object," Opt. Acta **28**, 357–367 (1981).
9. K. Patorski, "Self-imaging phenomenon lateral shift of Fresnel images," Opt. Acta **30**, 1255–1258 (1983).
10. H. Hamam and J. L. d. B. de la Tocnaye, "Fractional Talbot four-level phase-only holograms using ferroelectric liquid-crystal spatial light modulators," Opt. Lett. **19**, 1654–1656 (1994).
11. H. Hamam, "Talbot imaging and unification," Appl. Opt. **42**, 7052–7059 (2003).
12. H. Hamam, "Talbot array illuminators: general approach," Appl. Opt. **36**, 2319–2327 (1997).
13. P. Szwaykowski, "The lateral shift of Fresnel images of periodic objects under coherent plane wave illumination," Opt. Acta **31**, 563–566 (1984).
14. S. Bhattacharya and R. Sirohi, "Amplitude checker grating from one-dimensional Ronchi grating and its application to array generation," Appl. Opt. **36**, 3745–3752 (1997).
15. T. Cerda, U. Ruiz, D. Sánchez-de-la Llave, and V. Arrizon, "Simple techniques to generate binary periodical polarization fields," Appl. Opt. **59**, 6155–6160 (2020).

16. H. F. Talbot, "Facts relating to optical science. No. IV," Philos. Mag. **9**(56), 401–407 (1836).

17. M. V. Berry and S. Klein, "Integer, fractional and fractal Talbot effects," J. Mod. Opt. **43**, 2139–2164 (1996).

18. J. Azaña and M. A. Muriel, "Temporal self-imaging effects: theory and application for multiplying pulse repetition rates," IEEE J. Sel. Top. Quantum Electron. **7**, 728–744 (2001).

19. L. A. Hall, S. Ponomarenko, and A. F. Abouraddy, "Temporal Talbot effect in free space," Opt. Lett. **46**, 3107–3110 (2021).

20. A. Malacarne and J. Azaña, "Discretely tunable comb spacing of a frequency comb by multilevel phase modulation of a periodic pulse train," Opt. Express **21**, 4139–4144 (2013).

21. J. Azaña and H. G. de Chatellus, "Angular Talbot effect," Phys. Rev. Lett. **112**, 213902 (2014).

22. P. Szwaykowski, "Self-imaging in polar coordinates," J. Opt. Soc. Am. A **5**, 185–191 (1988).

23. D. Hebri, M. Bagheri, and S. Rasouli, "Talbot effect of azimuthally periodic Bessel-based structures," Opt. Lett. **44**, 4355–4358 (2019).

24. M. Yeganeh, S. Rasouli, M. Dashti, S. Slussarenko, E. Santamato, and E. Karimi, "Reconstructing the Poynting vector skew angle and wavefront of optical vortex beams via two-channel moiré deflectometry," Opt. Lett. **38**, 887–889 (2013).

25. M. Kumar and J. Joseph, "Optical generation of a spatially variant two-dimensional lattice structure by using a phase only spatial light modulator," Appl. Phys. Lett. **105**, 051102 (2014).

26. M. Sakamoto, K. Oka, R. Morita, and N. Murakami, "Stable and flexible ring-shaped optical-lattice generation by use of axially symmetric polarization elements," Opt. Lett. **38**, 3661–3664 (2013).

27. L. Ma and S. A. Ponomarenko, "Optical coherence gratings and lattices," Opt. Lett. **39**, 6656–6659 (2014).

28. Y. Chen, S. A. Ponomarenko, and Y. Cai, "Experimental generation of optical coherence lattices," Appl. Phys. Lett. **109**, 061107 (2016).

29. D. Hebri and S. Rasouli, "Diffraction from two-dimensional orthogonal nonseparable periodic structures: Talbot distance dependence on the number theoretic properties of the structures," J. Opt. Soc. Am. A **36**, 253–263 (2019).

30. B. Knyazev, O. Kameshkov, N. Vinokurov, V. Cherkassky, Y. Choporova, and V. Pavelyev, "Quasi-Talbot effect with vortex beams and formation of vortex beamlet arrays," Opt. Express **26**, 14174–14185 (2018).

31. S. Rasouli and D. Hebri, "Theory of diffraction of vortex beams from 2D orthogonal periodic structures and Talbot self-healing under vortex beam illumination," J. Opt. Soc. Am. A **36**, 800–808 (2019).

32. I. A. Kotelnikov, O. E. Kameshkov, and B. A. Knyazev, "Diffraction of Bessel beams on 2D amplitude gratings—a new branch in the Talbot effect study," J. Opt. **22**, 065603 (2020).

33. S. Schwarz, C. Kapahi, R. Xu, A. R. Cameron, D. Sarenac, J.-P. W. MacLean, K. B. Kuntz, D. G. Cory, T. Jennewein, K. J. Resch, and D. A. Pushin, "Talbot effect of orbital angular momentum lattices with single photons," Phys. Rev. A **101**, 043815 (2020).

34. D. Hebri and S. Rasouli, "Theoretical study on the diffraction-based generation of a 2D orthogonal lattice of optical beams: physical bases and application for a vortex beam multiplication," J. Opt. Soc. Am. A **39**, 1694–1711 (2022).

35. S. Rasouli, A. M. Khazaei, and D. Hebri, "Talbot carpet at the transverse plane produced in the diffraction of plane wave from amplitude radial gratings," J. Opt. Soc. Am. A **35**, 55–64 (2018).

36. S. Rasouli, A. M. Khazaei, and D. Hebri, "Radial carpet beams: a class of nondiffracting, accelerating, and self-healing beams," Phys. Rev. A **97**, 033844 (2018).

37. D. Hebri and S. Rasouli, "Combined half-integer Bessel-like beams: a set of solutions of the wave equation," Phys. Rev. A **98**, 043826 (2018).

38. S. Rasouli, S. Hamzeloui, and D. Hebri, "Colorful radial Talbot carpet at the transverse plane," Opt. Express **27**, 17435–17448 (2019).

39. D. Hebri, S. Rasouli, and M. Yeganeh, "Intensity-based measuring of the topological charge alteration by the diffraction of vortex beams from amplitude sinusoidal radial gratings," J. Opt. Soc. Am. B **35**, 724–730 (2018).

40. M. Yessenov, L. A. Hall, S. A. Ponomarenko, and A. F. Abouraddy, "Veiled Talbot effect," Phys. Rev. Lett. **125**, 243901 (2020).

41. K. Zhan, L. Dou, R. Jiao, W. Zhang, and B. Liu, "Talbot effect in arrays of helical waveguides," Opt. Lett. **46**, 322–325 (2021).

42. F. J. Torcal-Milla and L. M. Sanchez-Brea, "Diffraction by gratings with random fill factor," Appl. Opt. **56**, 5253–5257 (2017).

43. R. Jiao, L. Dou, W. Zhang, and K. Zhan, "Trajectory manipulation of Talbot images via dynamic linear index potentials," J. Opt. Soc. Am. B **38**, 123–128 (2021).

44. A. A. Goloborodko, "Effect of nonuniform pit structure on self-imaging of periodical gratings," J. Opt. Soc. Am. A **39**, 517–522 (2022).

45. K. Zhan, W. Zhang, R. Jiao, and B. Liu, "Period-reversal accelerating self-imaging and multi-beams interference based on accelerating beams in parabolic optical potentials," Opt. Express **28**, 20007–20015 (2020).

46. B. E. Saleh and M. C. Teich, *Fundamentals of Photonics* (Wiley, 2019).

47. P. Amiri, A. M. Dezfouli, and S. Rasouli, "Efficient characterization of optical vortices via diffraction from parabolic-line linear gratings," J. Opt. Soc. Am. B **37**, 2668–2677 (2020).

48. S. Rasouli, P. Amiri, V. V. Kotlyar, and A. A. Kovalev, "Characterization of a pair of superposed vortex beams having different winding numbers via diffraction from a quadratic curved-line grating," J. Opt. Soc. Am. B **38**, 2267–2276 (2021).

49. S. Rasouli, S. Fathollazade, and P. Amiri, "Simple, efficient and reliable characterization of Laguerre-Gaussian beams with non-zero radial indices in diffraction from an amplitude parabolic-line linear grating," Opt. Express **29**, 29661–29675 (2021).

50. H. Kogelnik, "Filter response of nonuniform almost-periodic structures," Bell Syst. Tech. J. **55**, 109–126 (1976).

51. F. Ouellette, "Dispersion cancellation using linearly chirped Bragg grating filters in optical waveguides," Opt. Lett. **12**, 847–849 (1987).

52. J. Yang, X. Hu, P. Xu, X. Lv, C. Zhang, G. Zhao, H. Zhou, and S. Zhu, "Chirped-quasi-periodic structure for quasi-phase-matching," Opt. Express **18**, 14717–14723 (2010).

53. Y. Wu, R. Ni, Z. Xu, Y. Wu, X. Fang, D. Wei, X. Hu, Y. Zhang, M. Xiao, and S. Zhu, "Tunable third harmonic generation of vortex beams in an optical superlattice," Opt. Express **25**, 30820–30826 (2017).

54. K. Dai, C. Gao, L. Zhong, Q. Na, and Q. Wang, "Measuring OAM states of light beams with gradually-changing-period gratings," Opt. Lett. **40**, 562–565 (2015).

55. D. N. Maywar and G. P. Agrawal, "Effect of chirped gratings on reflective optical bistability in DFB semiconductor laser amplifiers," IEEE J. Quantum Electron. **34**, 2364–2370 (1998).

56. N. Chen, Y. Nakano, K. Okamoto, K. Tada, G. I. Morthier, and R. G. Baets, "Analysis, fabrication, and characterization of tunable DFB lasers with chirped gratings," IEEE J. Sel. Top. Quantum Electron. **3**, 541–546 (1997).

57. A. M. Gillooly, H. Dobb, L. Zhang, and I. Bennion, "Distributed load sensor by use of a chirped moiré fiber Bragg grating," Appl. Opt. **43**, 6454–6457 (2004).

58. F. Mitschke and U. Morgner, "The temporal Talbot effect," Opt. Photon. News **9**(6), 45–47 (1998).

59. J. Azaña and L. R. Chen, "General temporal self-imaging phenomena," J. Opt. Soc. Am. B **20**, 1447–1458 (2003).

60. S. Rasouli, D. Hebri, and A. M. Khazaei, "Investigation of various behaviors of near-and far-field diffractions from multiplicatively separable structures in the *x* and *y* directions, and a detailed study of the near-field diffraction patterns of 2D multiplicatively separable periodic structures using the contrast variation method," J. Opt. **19**, 095601 (2017).

61. S. Rasouli and D. Hebri, "Contrast enhanced quarter-Talbot images," J. Opt. Soc. Am. A **34**, 2145–2156 (2017).

62. I. Amidror, *The Theory of the Moiré Phenomenon: Volume I: Periodic Layers* (Springer, 2009), Vol. **38**.

63. J. W. Goodman, *Introduction to Fourier Optics* (Roberts & Company, 2005).

64. P. Massoud Salehi and J. Proakis, *Digital Communications* (McGraw-Hill Education, 2007).

65. J. O. Smith, *Mathematics of the Discrete Fourier Transform (DFT): With Audio Applications* (Julius Smith, 2008).

66. H. J. Weber and F. E. Harris, *Mathematical Methods for Physicists: A Comprehensive Guide* (Academic, 2013).

67. S. Rasouli and P. Amiri, "Adjustable amplitude-phase hybrid gratings: intensity-sharing management between diffraction orders," OSA Contin. **3**, 2086–2095 (2020).
68. P. Zhou and J. H. Burge, "Analysis of wavefront propagation using the Talbot effect," Appl. Opt. **49**, 5351–5359 (2010).
69. K. Patorski, L. Wronkowski, and M. Dobosz, "Some properties of Fresnel images of a square wave amplitude grating," Opt. Acta **29**, 565–567 (1982).